

THESIS FOR THE DEGREE OF DOCTOR OF PHILOSOPHY

A database of single scattering properties for
hydrometeors at microwave and sub-millimetre
frequencies

Robin Ekelund



Department of Space, Earth and Environment
CHALMERS UNIVERSITY OF TECHNOLOGY
Göteborg, Sweden 2020

A database of single scattering properties for hydrometeors at microwave and sub-millimetre frequencies

ROBIN EKELUND

ISBN 978-91-7905-279-9

© ROBIN EKELUND, 2020.

Doktorsavhandlingar vid Chalmers tekniska högskola

Ny serie nr 4746

ISSN 0346-718X

Department of Space, Earth and Environment

Chalmers University of Technology

SE-412 96 Göteborg, Sweden

Telephone + 46 (0) 31 – 772 1000

Cover:

Rendering of aggregate particles simulated in a stochastic fashion, meant to represent snow. A short description of the software used for generating the aggregates is given in Sec. 3.8.

Typeset by the author using L^AT_EX.

Printed by Chalmers Reproservice

Göteborg, Sweden 2020

A database of single scattering properties for hydrometeors at microwave and sub-millimetre frequencies

ROBIN EKELUND

Department of Space, Earth and Environment

Chalmers University of Technology

Abstract

Remote sensing observations of hydrometeors (ice or liquid water particles) at microwave and sub-millimetre wavelengths provide important input to numerical weather forecasting through data assimilation and give insight to cloud processes that are relevant for climate prediction. The utilization of such measurements requires information on the single scattering properties (SSP), i.e., knowledge on how single hydrometeors scatter, absorb, and emit radiation. However, SSP are dependant on the particle orientation, shape, and size which in the case of ice hydrometeors are highly variable in nature. Furthermore, simulating the SSP of hydrometeors is challenging and computationally costly. These are the main challenges that this thesis aims to address.

In the first study of this thesis, a new publicly available SSP database for randomly oriented ice hydrometeors was developed. In terms of covered frequencies, temperatures, sizes, and particle models it is the most extensive to date. Particle models include aggregates that were generated using a semi-realistic, stochastic aggregation simulator. The next study utilised the simulator for a more detailed investigation on the dependence of SSP upon aggregate characteristics. For instance, the size and aspect ratio of the constituent crystals were found to have a significant impact on the extinction and back-scattering cross-sections of the aggregates. The third study analysed the ability of the SSP database to reproduce a combination of real passive and active satellite observations, by the GPM (Global Precipitation Measurements) Microwave Imager (GMI) and the CloudSat Cloud Profiling Radar, in radiative transfer (RT) simulations. While the tested particle models could accurately reproduce the real observations, it was difficult to find a particle model that performed better than the others. However, complementary simulations show promise with respect to the upcoming Ice Cloud Imager. In the fourth study, SSP of ice particles that have a preference towards horizontal orientation were calculated and applied to passive RT simulations at 166 GHz. The characteristic polarization signals present in GMI observations of clouds were successfully reproduced by RT simulations. The final study provides SSP of non-spheroidal rain drops, accounting for the effect of aerodynamic pressure upon the drop shape. It was found that this effect can have a small, but non-negligible, impact on passive and active microwave observations.

Keywords: Hydrometeors, clouds, water vapour, single scattering properties, microwaves, sub-millimetres, remote sensing, satellites.

Acknowledgments

First of all, thanks goes to Prof. Patrick Eriksson and Prof. Donal Murtagh for accepting me into the global environmental measurements and modelling group (GEMM) (which does not exist any more). These five years in my life have meant a lot to me; the return to my birthplace, the introduction to a completely new research field, and meeting my future wife. As my supervisor, Patrick Eriksson always found time for guidance, support, and encouragement. For that I am forever grateful. Thanks also goes to all of my colleagues in the GEMM group and the division of microwave and optical remote sensing, who made me feel welcome and made the department such a pleasant workplace.

Special thanks goes to my co-supervisor Michael Kahnert, Torbjörn Rathsmann who developed the snowflake tool-kit software as his master's project, and Manfred Brath for his work in the development of the oriented scattering data. The work has in large parts been done in collaboration with the remote sensing group at the Meteorological Institute, Hamburg University, who have my thanks for their work and support. Thanks to Vasileios Barlakas, Franz Kanngießer, Luisa Ickes, and Simon Pfreunds Schuh for providing feedback to this thesis.

Thanks to friends, old and new, for the good times we've had. Thanks to my family for their support. You've always let me follow my own path in life. Finally, thanks to my dear Shikha for your love, support, and kindness. I wouldn't have made it this far without you.

List of publications

This thesis is based on the following appended papers:

Paper A. P. Eriksson, R. Ekelund, J. Mendrok, M. Brath, O. Lemke, and S.A. Buehler (2018). “A general database of hydrometeor single scattering properties at microwave and sub-millimetre wavelengths”. *Earth System Science Data*, 10, pp. 1301–1326.

Paper B. R. Ekelund and P. Eriksson (2019). “Impact of ice aggregate parameters on microwave and sub-millimetre scattering properties”. *Journal of Quantitative Spectroscopy & Radiative Transfer*, 224, pp. 233–246.

Paper C. R. Ekelund, P. Eriksson, and S. Pfreunds Schuh (2020). “Using passive and active microwave observations to constrain ice particle models”. *Atmospheric Measurement Techniques*, 13, pp. 501–520.

Paper D. M. Brath, R. Ekelund, P. Eriksson, O. Lemke, and S. A. Buehler (2020). “Microwave and submillimeter wave scattering of oriented ice particles”. *Atmospheric Measurement Techniques*. Under review. Status: minor revision (AMT Discussions).

Paper E. R. Ekelund, P. Eriksson, and M. Kahnert (2020). “Microwave single scattering properties of non-spheroidal rain drops”. *Atmospheric Measurement Techniques*. Manuscript submitted.

Other relevant publications co-authored by Robin Ekelund:

Fox, S., Mendrok, J., Eriksson, P., Ekelund, R., O’Shea, S. J., Bower, K. N., Baran, A. J., Chawn Harlow, R., and Pickering, J. C. (2019). *Airborne validation of radiative transfer modelling of ice clouds at millimetre and sub-millimetre wavelengths*. *Atmospheric Measurement Techniques*, 12, pp. 1599–1617.

Pfreunds Schuh, S., Eriksson, P., Buehler, S. A., Brath, M., Duncan, D., Larsson, R., and Ekelund, R. (2019). *Synergistic radar and radiometer retrievals of ice hydrometeors*. *Atmospheric Measurement Techniques*. Under review.

Contents

Abstract	i
Acknowledgments	iii
List of publications	v
I Introductory chapters	1
1 Introduction	3
1.1 Background	3
1.2 Single scattering properties	5
1.3 This thesis	5
2 Atmosphere of Earth	7
2.1 The ideal gas law	7
2.2 Structure and composition	8
2.3 Water vapour	10
2.4 Clouds	11
2.5 Precipitation	14
2.6 Atmospheric water in weather and climate	14
3 Hydrometeor microphysics	17
3.1 In-situ measurement techniques	17
3.2 The birth of hydrometeors	19
3.3 The growth of hydrometeors	20
3.4 Frequency of observed ice particle types	25
3.5 Particle characterisation	26
3.6 The particle size distribution	27
3.7 Particle orientation	29
3.8 Shape data	30

4	Atmospheric radiative transfer	35
4.1	Electromagnetic wave propagation	36
4.2	Scattering and absorption by particles	39
4.3	Thermal radiation	44
4.4	The radiative transfer equation	46
4.5	Input data	47
4.6	Solving the radiative transfer equation	50
5	Microwave and sub-millimetre remote sensing	55
5.1	Platforms	55
5.2	Active remote sensing	57
5.3	Passive remote sensing	58
6	Summary and outlook	61
6.1	Paper A	61
6.2	Paper B	61
6.3	Paper C	62
6.4	Paper D	63
6.5	Paper E	63
6.6	Conclusions and outlook	64
6.7	Contribution to papers	65
	Bibliography	67
II	Appended papers	75
A	A general database of hydrometeor single scattering properties at microwave and sub-millimetre wavelengths	77
B	Impact of ice aggregate parameters on microwave and sub-millimetre scattering properties	105
C	Using passive and active microwave observations to constrain ice particle models	121
D	Microwave and submillimeter wave scattering of oriented ice particles	143
E	Microwave single scattering properties of non-spheroidal rain drops	175

Part I

Introductory chapters

Chapter 1

Introduction

1.1 Background

Clouds consist of water vapour and hydrometeors (water particles) that can be either liquid or frozen. As clouds cover about two thirds of Earth on average (Wylie et al., 2005; Stubenrauch et al., 2013), it is difficult to exaggerate their importance and impact on the environment of Earth. By reflecting incoming solar radiation out to space and trapping outgoing longwave radiation emitted from Earth's surface and atmosphere, clouds regulate Earth's temperature through radiative forcing. They also influence atmospheric and climate dynamics. For instance, the formation of clouds warms the atmosphere through heat of condensation, driving atmospheric circulation (Bony et al., 2015). As a part of the hydrological cycle, they are precursors to precipitation. The annual monsoon systems (seasonal changes in atmospheric circulation and precipitation) are important for a large fraction of the human population, as their variation can have detrimental effect on agriculture due to either lack or excess of rainfall (Webster et al., 1998).

The climate of Earth is changing. Multiple evidence provided through observations of the oceans, land, and atmosphere show that we, humans, are responsible by our continued release of anthropogenic greenhouse gases into the atmosphere (IPCC, 2013b). The question is no longer if global warming can be prevented. The global surface temperature is predicted to rise for several more decades, even in the event of a full stop of greenhouse gas emission today (IPCC, 2013c). The urgency is therefore shifting towards preparation and mitigation. The understanding and ability to predict how cloud processes vary in time and respond to a warming climate is of crucial importance in this respect.

However, much uncertainty exists around the radiative forcing and dynamics of clouds, which are complex systems and difficult to represent in numerical models. Climate and weather prediction are performed through so called global circulation models (GCMs). Cloud processes, which occur on scales from micrometres to thousands of kilometres, are virtually impossible to resolve in such configurations. Small scale processes must instead be represented through parameterisations. Errors or failure to capture the variability of said processes will lead to errors in weather and climate forecasting.

Ice hydrometeors stand out in this respect. It is often said that no two snowflakes are alike and this is close to the truth. While liquid hydrometeors are typically spherical or spheroidal in the case of rain, snow and ice crystals found in cold clouds take on an incredible range of different shapes. This is due to their solid form and the variety of processes involved in their formation. Ice particles can also be oriented in multiple ways, further complicating the situation. These aspects influence and complicate their interaction with electromagnetic radiation, making it difficult to relate the measured radiation to the mass of clouds or precipitation. Indeed, so called cirrus clouds, high altitude ice clouds, remain a particular source of uncertainty in GCMs in terms of their radiative effects (Baran, 2009).

More information on ice hydrometeors and their global distribution are needed. The latter can only be achieved through satellite remote sensing, i.e. measurements of the electromagnetic radiation emitted and scattered by Earth. Such observations are valuable in several ways (Duncan and Eriksson, 2018). In numerical weather prediction (NWP), Earth observations are used to constrain the model to reality, by comparing them to simulated observations. Through retrievals, i.e., the mapping of measurements to the physical quantities of interest, understanding of atmospheric processes and phenomena important for climatology can be gained. Furthermore, global observations provide a reference that can be used to evaluate climate models.

Satellite sensors using visible and infrared wavelengths have observed coverage and radiative forcing of clouds for decades. But at such wavelengths the radiation can not penetrate far into the clouds and as a consequence provides limited information on the vertical profile and mass of the clouds. Microwave frequencies are much more suited for this, as they can penetrate the clouds and still provide sensitivity to the ice particles. Microwave observations have dramatically risen in importance for the forecasting ability of the European Centre for Medium-range Weather Forecasts (ECMWF) (Geer et al., 2017). Much credit goes towards the improved ability of the data assimilation system to consider satellite observations that are affected by hydrometeors (cloudy radiances). Such measurements contain valuable information on the dynamical state of the atmosphere. Future satellite sensors, such as the Ice Cloud Imager (ICI) aboard the upcoming European polar orbiting weather satellites, will extend operational sensors into sub-millimetre wavelengths (Eriksson et al., 2020). Because these sub-millimetre wavelengths are closer to the typical sizes of ice hydrometeors, they provide additional sensitivity to smaller ice particles.

The utilisation of microwave remote sensing measurements in data assimilation and retrievals in the context outlined above requires an understanding in how the ice particles interact with the microwave and sub-millimetre radiation. Particles can absorb, scatter, and emit radiation. These processes are often collected under a single umbrella term, *single scattering properties* (SSP). If the assumed SSP do not sufficiently match reality, forecasting or retrieval errors arise. Traditionally, ice particles have been modelled as spheres or spheroids (Eriksson et al., 2015). However, it has become clear that such simplified assumptions can not represent the microwave SSP of ice particles with sufficient accuracy when multi-frequency observations are considered (Geer and Baordo, 2014). In short, more advanced representations of the microwave and sub-millimetre SSP of ice hydrometeors are needed. This is the

issue that this Ph.D. project aims to address. In specific, the focus is towards SSP of particles with realistic shapes, sizes, and orientations, as well as supporting upcoming missions by extending the coverage to higher frequencies.

1.2 Single scattering properties

Microwave and sub-millimetre SSP are difficult to determine empirically for practical reasons. Instead, the SSP are simulated. Two main steps are involved in the calculation of SSP:

1. Generation of shape data. Shape data describe the physical shape of the particles that are to be modelled. It should represent the particles accurately and it is required that the shape data can be used as input to the SSP calculation algorithm.
2. Calculation of the SSP. The interaction between incident electromagnetic radiation and a single particle is simulated at the required frequencies, temperatures, particle sizes, etc. The SSP can then be calculated as a set of parameters usable as input to radiative transfer (TR) modelling.

1.3 This thesis

The overarching goal of this Ph.D. project has been to establish full coverage of the SSP of hydrometeors, not only frozen ones, in the microwave and sub-millimetre wavelength regions. This thesis is the culmination and documentation of that work.

Part I, which consists of six chapters, serves as an introduction of the research carried out in the Ph.D. project. Chapter 2 overviews the atmosphere in relation to water vapour and clouds, serving as context for the work as a whole. Chapter 3 covers the microphysics of hydrometeors, relevant for the generation of shape data and the other aspects relevant for particle SSP. Chapter 4 discusses radiative transfer, with a focus on SSP properties. Chapter 5 gives an overview of remote sensing and Chapter 6 summarises the papers.

In Part II, a compilation of all the included papers that describe the research is provided. In paper A, the complicated and varied shapes of ice particles were considered and their SSP calculated and stored in an extensive, publicly available database, for the benefit of the remote sensing community. In paper B, the physical properties of modelled ice aggregates and their consequent impact upon SSP were investigated. Paper C employed the SSP database in radiative transfer simulations for the purpose of testing and validation. In paper D, the work in paper A was continued by calculating the SSP of ice particles that are oriented, which is important for polarimetric observations. Finally, in paper E the scope was broadened with the inclusion of SSP calculations of non-spheroidal liquid hydrometeors.

Chapter 2

Atmosphere of Earth

Earth's atmosphere is the layer of gas that surrounds our planet. Understanding its dynamics and interaction with the other systems of Earth is of high socio-economic importance. Weather forecasting has historically been a main motivator for atmospheric research and has as a consequence provided much of the infrastructure (satellite instruments, weather radars, computational centres, etc.), driving the field forward. As the impact of human activity upon the climate has become increasingly apparent, the field of climate dynamics has further promoted atmospheric research.

In order to contextualise the work done in this thesis, an overview of the atmosphere and its components is given in this chapter. The topic of this thesis is the radiative properties of liquid and frozen water particles, which are predominantly found in the troposphere, the lower part of the atmosphere. The focus of this chapter therefore lies at the troposphere and one of its most important components, water.

2.1 The ideal gas law

A large part of atmospheric dynamics can be understood and explained through the theory of thermodynamics. The *ideal gas equation* describes the state of an ideal gas¹. It gives the relationship between the temperature T and pressure p of a gas with volume V . The law comes in several forms, for instance

$$pV = nRT, \quad (2.1)$$

where n is the number of moles of the gas and R is the *universal gas constant*, which applies to any gas ($R = 8.3145 \text{ J K}^{-1} \text{ mol}^{-1}$). When considering air in the atmosphere, it is more convenient to consider the density ρ rather than n . Since $n = \frac{m}{M}$, where m is the mass of the gas and M is the molar mass of the medium, Eq. 2.1 can be rewritten as

$$p = \frac{\rho RT}{M}. \quad (2.2)$$

Equation 2.2 can be applied to both homogeneous gas mixtures (such as air) and the individual components of the mixture (assuming that the gas components are not

¹A theoretical *ideal gas* is composed of point particles which only interact through perfectly elastic collisions. Air can be treated as an ideal gas at standard atmospheric conditions.

chemically reacting with each other). As such, the total pressure p in air is the sum of the *partial pressures* p_i acted by all gas components. Due to the high variance of water vapour within the atmosphere, it is often convenient to consider the pressure of dry air p_d and water vapour p_{wv} separately. The total pressure is then

$$p = p_d + p_{wv}. \quad (2.3)$$

2.2 Structure and composition

The atmosphere consists of a gas known as air, a gas mixture of 78.08% nitrogen (N_2), 20.95% oxygen (O_2), and 0.93% argon (Ar) (Wallace and Hobbs, 2006). Up to an altitude of approximately 100 km, this mixture tends to be fairly uniform throughout the atmosphere thanks to turbulent mixing. Some trace gases, such as carbon dioxide (CO_2) and water vapour (H_2O), are exceptions to this rule. Water vapour is arguably most prominent example. Highly variable in the atmosphere, water vapour is mostly concentrated to the lower part of the atmosphere known as the *troposphere*. In the next section, water vapour will be covered in more detail.

The structure of the atmosphere is largely understood through its interaction with solar radiation and the theory of thermodynamics. It is composed of four layers based on the vertical distribution of temperature, as shown in Fig. 2.1. Above the surface resides the aforementioned troposphere. The surface is warmed by solar radiation and heat is transported up in the atmosphere through sensible heat, latent heat, and radiation. The troposphere is then cooled through emission of longwave radiation and is characterised by a decreasing temperature with height. The temperature decreases with an average *lapse rate* of approximately $6.5^\circ C km^{-1}$ (Wallace and Hobbs, 2006). The layer directly above the troposphere is called the *stratosphere*, having a positive lapse rate due to absorption of solar ultra-violet (UV) radiation by ozone. Similarly to water vapour, ozone is not well-mixed in the atmosphere, as a consequence of its production mechanisms and its propensity to react with other species. The boundary between the troposphere and stratosphere is called the tropopause, and is found at altitudes from 8 to 18 km. The positive lapse rate in the stratosphere strongly inhibits vertical mixing, and the interaction between the troposphere and stratosphere at the tropopause is therefore limited. The remaining layers are called the *mesosphere* and the *thermosphere*. The positive lapse rate within the thermosphere is due to absorption of solar radiation by nitrogen and oxygen.

The variation of pressure as a function of altitude can be understood by considering an atmosphere in hydrostatic balance and the ideal gas law. In an atmosphere in hydrostatic balance, the pressure force acting from below, on a thin horizontal layer of air, is balanced out by the pressure force acting from above and the weight of the air layer. This results in the following equation

$$\frac{\partial p}{\partial z} = -g\rho, \quad (2.4)$$

where z is the altitude, ρ is the air density, and g is the gravity acceleration of Earth

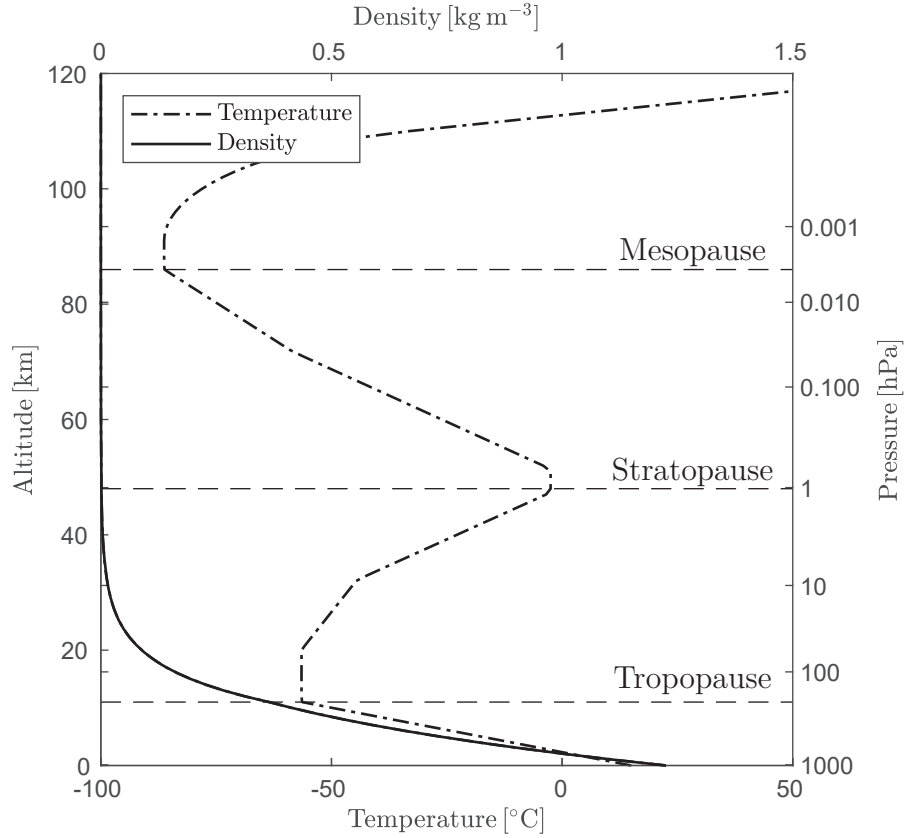


Figure 2.1: Temperature and density profiles. Temperature taken from the 1976 U.S. standard atmosphere (Minzner, 1977).

($g \approx 9.81 \text{ m s}^{-2}$). Inserting Eq. 2.2 into 2.4 gives

$$\frac{\partial p}{\partial z} = -\frac{gM}{RT}p. \quad (2.5)$$

The solution is given by

$$p(z) = p_0 \exp\left(-\frac{z}{H}\right), \quad (2.6)$$

where p_0 is the pressure at the zero altitude (mean sea level) and $H = \frac{RT}{gM}$ is the scale height. For the standard atmosphere, p_0 equals 1013.25 hPa. While the temperature is not constant in the atmosphere, it varies within a limited range (see Fig. 2.1). Assuming the mean temperature of the troposphere and the stratosphere is approximately 255 K and considering dry air with molar mass $M = 28.97 \text{ mol}$, the scale height is roughly 7.5 km. The pressure at various altitudes is indicated in the right axis of Fig. 2.1.

Equation 2.2 and 2.6 also yield the variation of density with altitude as

$$\rho(z) = \frac{p_0}{Hg} \exp\left(-\frac{z}{H}\right). \quad (2.7)$$

The density is plotted in Fig. 2.1.

2.3 Water vapour

Atmospheric water vapour is concentrated to the troposphere; about 99 % resides here. The high variability in concentration of water is related to the fact that water can exist in all its phases, gas, liquid, and solid, at pressures and temperatures found in the troposphere. The amount of water vapour in the air can be quantified in a number of ways. The vapour mixing ratio w is defined as

$$w = \frac{n_{\text{wv}}}{n_{\text{d}}} = \frac{p_{\text{wv}}}{p_{\text{d}}} = \frac{p_{\text{wv}}}{p - p_{\text{wv}}}, \quad (2.8)$$

where n_{wv} and n_{d} is the number of moles of water vapour and dry air in an unit volume, respectively. Equation 2.1 and 2.3 were used to rewrite w in terms of the partial pressures of vapour and dry air. w ranges from about 10 ppm (part per million) in the coldest and driest regions, to 5 % in the most humid and hot ones (Wallace and Hobbs, 2006).

More intuitive measures of humidity exist. Consider a liquid water surface and a layer of water vapour with temperature T above it. Simultaneously, water vapour condenses on the surface and surface water evaporates. At a certain partial water vapour pressure p_{ws} , the *saturation vapour pressure with respect to a water surface*, these processes balance out each other and the water vapour density is constant, i.e., the air is saturated with respect to a liquid water surface. As shown in Fig. 2.2, p_{ws} depends upon and increases with the temperature. The mixing ratio of saturated air is given by

$$w_{\text{s}} = \frac{p_{\text{ws}}}{p_{\text{d}}} = \frac{p_{\text{ws}}}{p - p_{\text{ws}}}. \quad (2.9)$$

As an example, at surface pressure and a temperature of 30 °C, w_{s} is 4.3 %. At 0 °C, w_{s} is instead 0.61 %, explaining the typically much drier air in colder regions.

The vapour concentration of air is not necessarily at equilibrium, but can be either below or above the saturation level, depending upon a number of factors. A typical measure of humidity is the relative humidity (RH), defined as

$$\text{RH} = 100 \frac{w}{w_{\text{s}}} [\%]. \quad (2.10)$$

It should be stressed that a relative humidity of 100 % does not mean that the air can not hold any more water vapour, it only means that the air is in equilibrium with respect to a water surface. In the absence of a water surface, liquid drops will not necessarily form even though RH is above 100 %, i.e., when the air is *supersaturated*. An overview of the mechanisms involved and conditions required for droplet formation is given in Sec. 3.2.

The concept of p_{ws} can also be applied to an ice surface, where the vapour *deposits* upon the ice and the ice simultaneously *sublimates* to vapour. At *saturation pressure with respect to an ice surface* p_{wsi} , these two processes are in balance. Figure 2.2 shows p_{wsi} in terms of its difference compared to p_{ws} . It is seen that below 0 °C, p_{wsi} is lower compared to p_{ws} , with a maximum difference of approximately 26.6 Pa at –11.8 °C. In certain conditions this is of great importance. Consider an air parcel

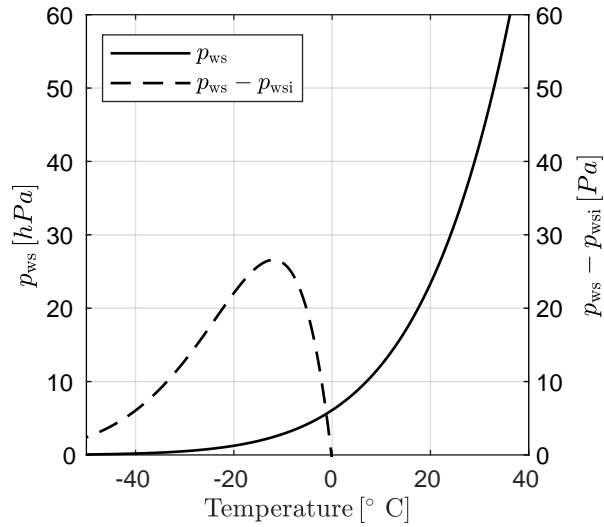


Figure 2.2: Saturation vapour pressure with respect to a liquid water surface p_{ws} in the black line. Also included is the difference between p_{ws} and the saturation pressure with respect to an ice surface p_{wsi} . p_{ws} is derived according to the Goff-Gratch equation and p_{wsi} according to Helten et al. (1999).

at sub-zero temperature, in contact with both a liquid and frozen surface. If the vapour pressure p_{wv} is higher than both p_{ws} and p_{wsi} , both surfaces will grow through condensation and deposition. As the vapour is depleted and the pressure reaches p_{ws} , the evaporation and condensation rates are in equilibrium and liquid surface growth stops. However, at this stage p_{wv} is still higher than p_{wsi} and deposition upon the ice surface continues. As a consequence, the ice surface continues to drain the air of vapour until p_{wsi} is reached. Since the vapour pressure is now below p_{ws} , the liquid surface will start to evaporate. The liquid surface will indirectly feed the ice surface with vapour until complete evaporation. This process is called the Wegener-Bergeron-Findeisen (WBF) process (Storelvmo and Tan, 2015) and is important in supercooled clouds that contain both liquid droplets and ice particles, so called mixed-phase clouds.

2.4 Clouds

Clouds are a vital component in Earth's atmosphere. On average, the global cloud fraction is approximately 0.56 when considering clouds of optical depth higher than 2 and 0.68 for clouds of optical depth higher than 0.1 (Stubenrauch et al., 2013). They regulate Earth's radiative budget and influence atmospheric circulation.

Cloud droplets can form when the air is saturated. This can happen either through cooling or moistening. Fogs, i.e., clouds that touch the ground, are often formed through moistening. For instance, when warm rain falls through cold air, drops evaporate and add moisture to the cold air, which in turn can form so called *precipitation fog*. Similarly, moistening can occur when cold air moves over a warm lake.

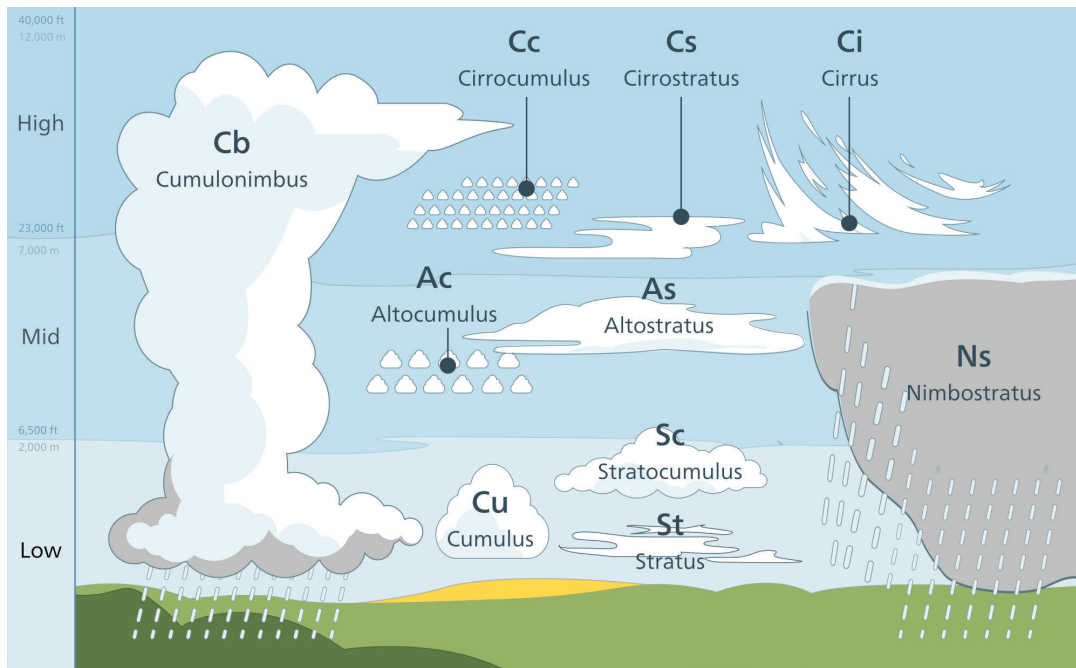


Figure 2.3: The main cloud types. Image taken from Wikipedia commons (https://commons.wikimedia.org/wiki/File:Cloud_types_en.svg, accessed 10 February 2020).

Clouds are typically associated with cooling. Air is lifted to higher altitudes due to instability and is cooled adiabatically, according to the ideal gas law (Eq. 2.1). As the air parcel cools, the saturation pressure decreases (see Fig. 2.2) and consequently the relative humidity increases. The morphology, i.e., shape and size of clouds, is determined by the conditions which lead to the lifting and cooling of the air. Two main types of clouds exist, *cumuliform* and *stratiform* clouds. An overview of typical clouds is found in Fig. 2.3.

Cumuliform clouds are active clouds, in the sense that they are formed in unstable air which raise vertically through buoyant forces. The convection can be driven by solar heating of the surface. Smaller cumuliform clouds have a puffy appearance, like cauliflowers or towers. Extreme cases of deep convection form thunderstorms that look like anvils or mushrooms, which can reach all the way up to the tropopause. The horizontal extension of cumuliform clouds is approximately the same as their height.

Stratiform clouds are passive since the buoyant force acts to suppress vertical growth, and the lifting occurs through other means. Clouds along warm fronts are typically stratiform. The warm air is raised along the front, adiabatically cooling it. As such, stratiform clouds are smooth with large horizontal coverage. They can also be formed through forced lifting by topographic features such as mountains, in which case they are labelled *orographic clouds*.

2.4.1 Ice clouds

We tend to think of clouds as liquid, considering the wetness we experience by the rain they produce. But high up in the atmosphere, at altitudes colder than -30° , clouds are pre-dominantly frozen. By horizontal coverage, the most common type is the so called *cirrus* clouds. The World Meteorological Organization (WMO) classifies cirrus based on their visual appearance in daylight. They are described as white, delicate filaments or white patches or narrow bands (Lynch et al., 2002). Typically, cirrus clouds exist above 8km and are colder than -30°C (Heymsfield et al., 2017). As indicated by Fig. 2.3, there are multiple type of cirrus, defined by their appearance and formation. The most common of these are cirrostratus, which generally extend horizontally in hundreds of kilometres. In the tropics, cirrus clouds are often formed from the top of cumulonimbus (i.e., thunderstorms) by wind shear. They are called *anvil* clouds and impose significant radiative forcing in the tropics due to their horizontal extension. Another important category of clouds very common in the tropics is sub-visual cirrus clouds, which are barely visible to the eye except under certain conditions. Perhaps counter-intuitively, as a consequence of their thinness they have significant impact upon the radiative balance of Earth (see Sec. 2.6 and 4.6.2 for details). Overall, the global average cirrus coverage is about 23%, but can be over 50% in the tropics (Heymsfield et al., 2017).

In principle, the cloud phase is determined by the temperature of the ambient air, i.e., below the zero isotherm hydrometeors are liquid and above they are frozen. This is mostly true for stable conditions such as for stratiform clouds. In case of convection or turbulence, liquid droplets can be lifted above the zero isotherm. Droplets colder than 0°C can persist as supercooled droplets. Ice particles typically melt quickly above 0°C . The convective core of cumulonimbus is typically composed of both liquid droplets and graupel or hail. Nimbostratus that reach high enough up into the atmosphere may also become partially glaciated at the cloud top.

2.4.2 Cloud characterisation

Apart from the classifications given in previous sections, there are several parameters relevant for the description of the properties of clouds. Horizontal and vertical extensions are measures that depend on definition and are often somewhat arbitrary. More practical and well-defined parameters are liquid water content (LWC) and liquid water path (LWP), which describe spatial distributions of liquid water mass, irrespective of how the cloud boundaries are defined. The liquid water content gives the mass of liquid water in an unit volume and is often given in units of g m^{-3} . The liquid water path is instead the column-integrated LWC, i.e., the amount of liquid water above a unit square meter. The unit of LWP is kg m^{-2} . For ice clouds, the same parameters are used, but are instead called ice water content (IWC) and ice water path (IWP).

Another important parameter is number density N , which in the context of liquid clouds gives the number of droplets in a volume element. The number density applies to ice clouds and precipitation as well. Because the hydrometeors in a cloud rarely are of a single size, one also has to consider the particle size distribution (PSD) of the

cloud. The PSD $\frac{\partial N}{\partial D}$ gives the number of particles per unit volume per unit particle size and has units of $\text{m}^{-1} \text{m}^{-3}$. To elaborate, if the particle size is given in terms of its diameter D , then the PSD gives the number of particles in the interval $[D, D + \Delta D)$ (larger or equal to D and less than $D + \Delta D$). A more in-depth discussion of PSDs and its implications is provided in Sec. 3.6.

Under the assumption that a cloud only has spherical droplets of a single diameter D (a monodisperse PSD), which is a reasonable approximation in certain conditions, LWC and N can be related to each other as

$$LWC = N \rho_{\text{lw}} \frac{\pi D^3}{6}, \quad (2.11)$$

where ρ_{lw} is the density of liquid water. For IWC, a similar expression can be given. However, one has to consider the fact that ice particles generally are not spherical.

2.5 Precipitation

Precipitation is an important part of the hydrological cycle that influences vegetation, storms, and weather in general. In essence, it is a generic term for hydrometeors that are heavy enough to fall towards the ground. Note that the hydrometeors do not necessarily have to reach the ground for it to be considered precipitation. *Virgas* are visible fallstreaks of precipitation that evaporate or sublimate before reaching the ground, redistributing humidity in the atmosphere.

The strength of precipitation, termed rain or snowfall, is typically given as the flux density of water in units of mm h^{-1} . Since the depth of ground snow depends on several factors such as snow shape and temperature, snowfall typically implies the amount of equivalent melted water. It is often the case that the rain water content (RWC) is considered, i.e., the amount of rain water mass in a volume element.

2.6 Atmospheric water in weather and climate

This chapter is concluded with a comment on the role of water in Earth's weather and climate. The importance of clouds to atmospheric circulation and hydrology was already emphasized in the Chapter 1. Focus is here put towards the impact of clouds on Earth's radiative budget.

Water vapour is a greenhouse gas. In terms of total contribution to the greenhouse effect, it is the most important one (Maurellis and Tennyson, 2003). Highly absorbing at infrared wavelengths, outgoing longwave radiation is absorbed by atmospheric vapour and partially directed back towards the surface, resulting in a net positive radiative forcing that warms Earth. In contrast to other prominent greenhouse gases, such as CO_2 , it is not considered as an anthropogenic gas. Water vapour does not control the greenhouse effect, rather, its abundance in the atmosphere is determined by atmospheric temperature and implicitly by the greenhouse effect. In a warming climate the water vapour concentration is expected to increase (consider the dependence of saturation pressure upon temperature in Fig. 2.2), which in turn

will amplify the greenhouse effect. As such, water vapour is important because it has a positive feedback effect on a warming climate (Rind et al., 1991; IPCC, 2007).

Clouds have feedback effects as well, but in a more complex manner and are much more difficult to quantify. The net radiative effect of clouds depends on the cloud height and optical thickness at different frequencies. Liquid clouds that are close to the surface reflect much of the incoming solar radiation, yielding a negative radiative forcing. While these clouds also trap outgoing longwave surface radiation, radiation emitted from the atmosphere above is not affected. The net radiative forcing is therefore generally negative. For optically thick cirrus or deep convective clouds, the radiative forcing is more difficult to quantify, because the clouds interact strongly with both the shortwave and longwave radiation. Sub-visual cirrus clouds may be transparent at visible wavelengths and semi-opaque at infrared wavelengths (see Sec. 4.6.2 for details), which produces a net positive forcing.

Quantifying the feedback of the different types of clouds is difficult, especially for ice clouds. As an example, many global circulation models (GCMs) predict less low clouds in a warming climate, so the feedback would in that case be positive (IPCC, 2013a). Furthermore, the amount and height of cirrus clouds are expected to increase, which would then lead to a positive feedback as well. The uncertainty is large however. More and better observations are needed in order to improve our knowledge on cloud feedback effects and reduce the uncertainty (Waliser et al., 2009; Duncan and Eriksson, 2018).

Chapter 3

Hydrometeor microphysics

Hydrometeors, i.e., atmospheric water particles, come in many shapes and sizes. Cloud droplets can be as small as $0.1\ \mu\text{m}$, while hailstones can reach sizes of several centimetres. Figure 3.1 exemplifies the span of hydrometeor sizes. Ice particles are furthermore distinguished by the extreme variability in shapes found in nature.

This chapter begins with an overview of in-situ techniques from which most of the knowledge on hydrometeor microphysics stems from. It continues with an overview of the *microphysics* of hydrometeors, i.e., the phenomena occurring at the microscopic scale (i.e., in the orders of μm) relevant for the nucleation, growth, and characterisation of liquid and frozen hydrometeors. This information culminates into a description of shape data, which is required to calculate the radiative properties of hydrometeors.

3.1 In-situ measurement techniques

In contrast to remote sensing, *in-situ* (literally Latin for *on site*) measurements are performed with instruments located directly at the point of interest. Such measurements are relevant to mention here, since they are the only option for retrieving detailed information on particle microphysics, such as particle shape and size. The in-situ techniques can be divided into groups of airborne and ground-based instrumentation.

Airborne in-situ measurements are vital for improving the understanding of ice particle microphysics because they can capture the different growth stages of the particles. Several types of airborne instruments exist and are in use. One family of instruments are the Optical Array Probes (OAP), which function by illuminating particles with a collimated laser and imaging the particle shadows created. Examples of instruments employing this method include the Cloud Particle Imager (CPI) for high-resolution imagery (Lawson et al., 2001), 2-Dimensional Stereo (2D-S) probes for stereoscopic images (Lawson et al., 2006), and High-Volume Precipitation Spectrometer (HVPS) for large particles (Lawson et al., 1998). Such probes can be operated both on-board aircraft and balloons. Probes mounted on aircraft typically face the problem of shattering of ice particles that hit the edges of the probe inlet, leading to an artificial increase in the concentrations of smaller ice crystals ($<100\ \mu\text{m}$).

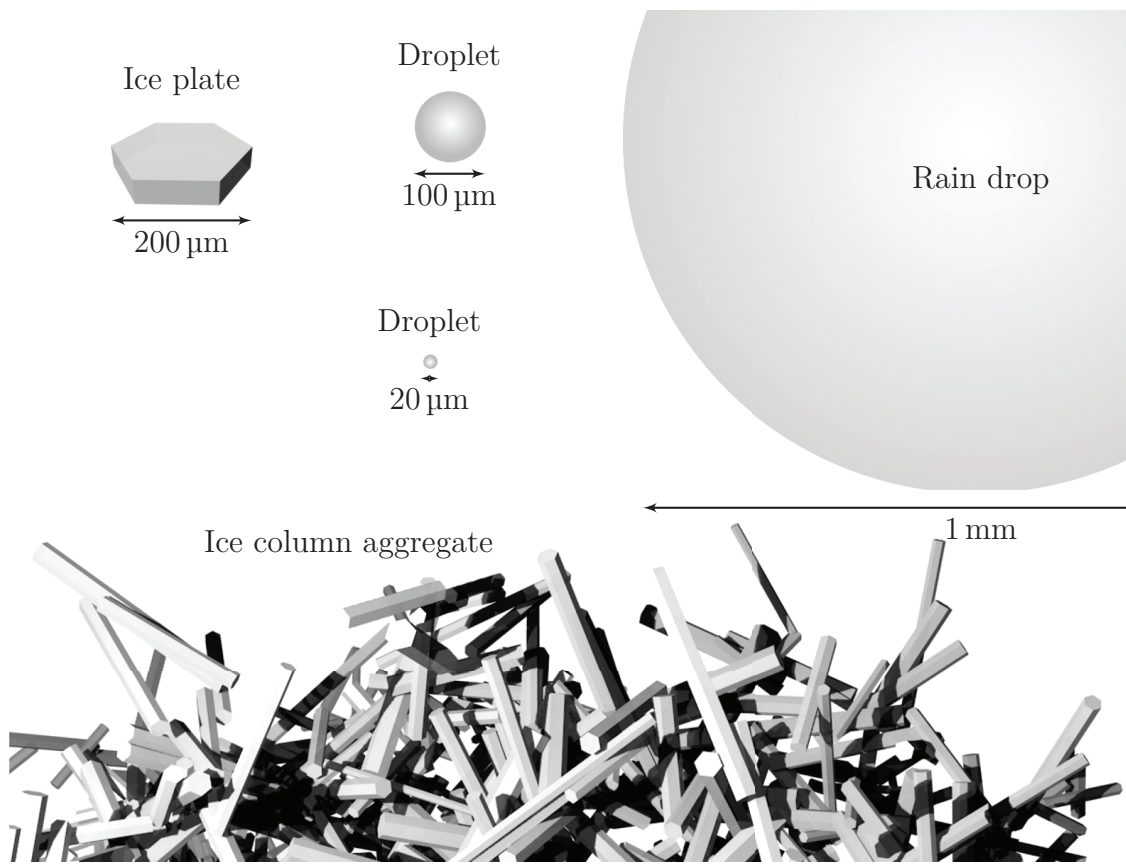


Figure 3.1: Comparison of typical hydrometeor sizes. Droplets of 20 and 100 μm are seen along with a rain drop of 1 mm. A hexagonal ice plate with a length of 200 μm , typical for cirrus clouds, is also displayed. Finally, the periphery of an ice column aggregate of size larger than 2 mm is seen at the bottom. All particles are drawn to scale.

This error has to be corrected for (Field et al., 2006) or reduced through specially modified probe tips (Korolev et al., 2011). Another problem is particles that are out-of-focus in the images and consequently wrongly characterised, leading to even more artefacts in measured size distributions (O’Shea et al., 2019). Ice shattering is avoided for balloon-borne probes, since the ascent rate is slow in comparison (Kuhn and Heymsfield, 2016).

The major limitation of airborne missions is their expensiveness in comparison to ground-based instrumentation, which can be operated continuously at relatively low costs. In addition to particle shape and size, they can also measure particle fall-speeds. They are however limited to precipitating particles due to their locality. The Multi-Angle Snowflake Camera (MASC) (Garrett et al., 2012) is an example of ground-based instrumentation that captures high-resolution images of hydrometeors at three different angles. Example MASC images of ice particles are shown in Sec. 3.3.3.

While not strictly in-situ, laboratory observations bear mentioning as well. For instance, ice particles can be grown in chambers under highly controlled conditions. It is therefore possible to characterise ice particle growth in various conditions (e.g.,

temperature and humidity) in high detail. While such data can be useful to infer how ice particles in nature could look like, one should keep in mind that the ideal conditions created in laboratories are rarely found in nature. In the remainder of this chapter, current knowledge of hydrometeor microphysics gained through in-situ observations is overviewed.

3.2 The birth of hydrometeors

Before a hydrometeor can grow to a rain drop or snowflake, it has to be formed from water vapour in a process called nucleation. As discussed in Sec. 2.4, the requirement for this to happen is that the air is supersaturated, either with respect to liquid or frozen water. However, often this is not enough. So called *homogeneous nucleation*, where the nucleation is completely unaided by other particles (aerosols), can happen if the air is significantly supersaturated (over 10 %). This is often not the case, and water droplets instead form through condensation upon aerosols, a process called *heterogeneous nucleation*. The aerosol is in this context labelled as a *nucleus*. The nucleation of liquid and frozen hydrometeors is to some extent analogous, but significant differences exist. The upcoming two subsections explain how liquid and frozen hydrometeors are formed.

3.2.1 Nucleation of liquid droplets

In homogeneous nucleation, a liquid embryo is formed through random collisions of vapour molecule clusters. For the embryo to grow to significant sizes, it must overcome a certain threshold size r or it will evaporate. This threshold size depends on the level of supersaturation; the higher the supersaturation the smaller r is (Wallace and Hobbs, 2006). In practice, supersaturation (with respect to a water surface) in the atmosphere rarely exceeds a few percent, and homogeneous nucleation in nature is therefore almost impossible.

Droplets instead form through heterogeneous nucleation with the aid of various types of aerosols. Aerosols with hygroscopic properties may allow a thin film of water to condense upon the surface. In the context of liquid nucleation, the aerosols are referred to as *cloud condensation nuclei* (CCN). Cloud condensation nuclei are generally abundant in the atmosphere, and supersaturation is always depleted before homogeneous nucleation becomes probable. However, their number concentration can have significant effects on the droplet size distribution. Some CCNs are soluble, i.e., they dissolve in water. The saturation vapour pressure is lower for solutions, leading to much lower required supersaturation compared to pure water droplets. The development of droplet formation will be discussed in Sec. 3.3.1.

3.2.2 Nucleation of ice crystals

Ice crystals can nucleate homogeneously or heterogeneously. Analogously to liquid homogeneous nucleation, ice embryos can form spontaneously in a supercooled droplet and grow if it reaches above the threshold size r . In contrast to liquid droplets, ice

particles forming through homogeneous nucleation are possible in the atmosphere, as long as the temperature is low enough, colder than -35°C .

At higher temperatures, ice embryos form through heterogeneous nucleation. The aerosols that facilitate growth of ice embryos are referred to as *ice nuclei*. Heterogeneous ice nucleation occurs in four basic modes of action. An ice nucleus immersed in a droplet may initiate freezing once the droplet cools below a certain material dependant critical temperature (depends on the aerosol material), a process referred to as *immersion freezing*. *Contact freezing* can happen if a supercooled pure liquid droplet comes into contact with an ice nucleus. Heterogeneous freezing can also happen through either condensation (vapour to liquid) or deposition (vapour to ice) upon the ice nucleus directly. In the case of *condensation freezing*, vapour condenses upon the nucleus and freezes immediately. In *deposition freezing*, the water vapour deposits on the ice nucleus immediately.

An ice nucleus may act in one or even all of the four freezing modes. In the latter case, it should be noted that the critical temperature for a given ice nucleus is not the same for all freezing modes. For instance, kaolinite (clay) has critical temperatures -5 , -10 , -19 , and -32°C for contact, condensation, deposition, and immersion freezing, respectively (Rolland, 2000). Contact freezing generally occurs at relatively high temperatures and is therefore the most likely nucleation process (Pruppacher and Klett, 1997; Rolland, 2000). Other types of ice nuclei than clay include mineral dust, bacteria or combustion products such as soot. In general, ice nuclei are limited to specific aerosols with certain criteria. For instance, aerosols that have similar molecular structures to ice are often good ice nuclei (Pruppacher and Klett, 1997). Other requirements include insolubility and that the nucleus is large enough. Particles that dissolve liquids can not provide the crystal structure for ice to form upon, and the particle must be similar or larger in size than the critical ice embryo radius r (in the order of $0.1\ \mu\text{m}$) or the ice embryo may sublime away.

3.3 The growth of hydrometeors

Once the hydrometeor has been formed, it can continue to grow through diffusion (condensation or deposition) as long as the ambient air is supersaturated. However, other growth processes are of vital importance to the general characteristics of hydrometeors as observed in nature.

3.3.1 Growth of cloud droplets and rain drops

Small droplets grow through condensation, which can be expressed through the following formula

$$\frac{\partial r}{\partial t} = \frac{1}{r} \frac{M_w D_v}{\rho_{lw} R} \left[\frac{p_{wv}(\infty)}{T(\infty)} - \frac{p_{wv}(r)}{T(r)} \right], \quad (3.1)$$

where r is the droplet radius, R is the gas constant, T is the temperature, M_w is the molar mass of water, D_v is diffusion constant for water vapour in air, p_{wv} is the vapour partial pressure, and ρ_{lw} is the density of liquid water (Pruppacher and Klett, 1997).

In the brackets, p_{wv} and T are evaluated far away and directly at the droplet radius r . The equation implies that the droplet growth decreases with radius. Considering the fact that evaporation is not considered in the equation, diffusion growth can therefore not support the growth of droplets much larger than about $10\ \mu\text{m}$ (Pruppacher and Klett, 1997; Wallace and Hobbs, 2006). As illustrated in Fig. 3.1 larger droplets and rain drops exist; there must exist other growth mechanisms which promotes the growth of large hydrometeors.

Droplets larger than $10\ \mu\text{m}$ grow through coalescence. Coalescence occurs when two droplets collide and form a new larger droplet. This can happen in turbulence or if the fall-speeds of the droplets differ. The latter is the case in a cloud volume that contains differently sized droplets. As an individual droplet gains in mass, it starts to fall and collect the smaller and slower droplets. To what extent droplets are actually captured by the *collector drop* depends on multiple factors. Droplets that are very small compared to the drop tend to follow the laminar flow around the drop and avoid capture. Also, intermediate sized droplets that collide tend to bounce of each other, because the impact energy deforms the droplets and creates an air gap in between them which prevents coalescence. If the drop and droplet are differently sized, the impact energy is not enough to deform the drop and coalescence can occur.

3.3.2 Ice cloud particles

Compared to the liquid phase, the solid phase of water offers a higher diversity in growth processes. At small sizes, the diffusion growth can be expressed similarly to Eq. 3.1, except it has to be modified in order to account for non-sphericity of ice crystals. At sub-zero temperatures, deposition growth is preferred over condensation, because supersaturation with respect to liquid water is lower compared to supersaturation with respect to ice, as shown in Fig. 2.2. The Wegener-Bergeron-Findeisen (WBF) process (discussed in Sec. 2.3), is an important mechanism for ice formation that allows for ice particles to grow at the expense of liquid droplets in a supercooled mixed cloud. For instance, if the temperature is $-20\ \text{K}$ with 0% supersaturation with respect to liquid water, the supersaturation with respect to ice is 21% , which highly promotes deposition growth.

For diffusion growth the molecular lattice structure of ice influences the shape of the ice crystal. At conditions typical for the atmosphere, ice has a hexagonal lattice structure, explaining why snowflakes typically have six arms or the hexagonal appearance of ice columns and plates. Other structures such as cubic lattices are possible at very low temperatures ($< -80\ \text{°C}$), which is typically not the case in the troposphere.

Laboratory and in-situ observations show that the manner, in which ice particles grow in, is primarily influenced by temperature and secondarily by ice supersaturation, effectively determining the ice crystal type. Figure 3.2 demonstrates the variability of ice particle morphology with temperature and ice supersaturation. The images originate from a combination of laboratory results and in-situ observations using high resolution imagers (Bailey and Hallett, 2009). Determined by the temperature

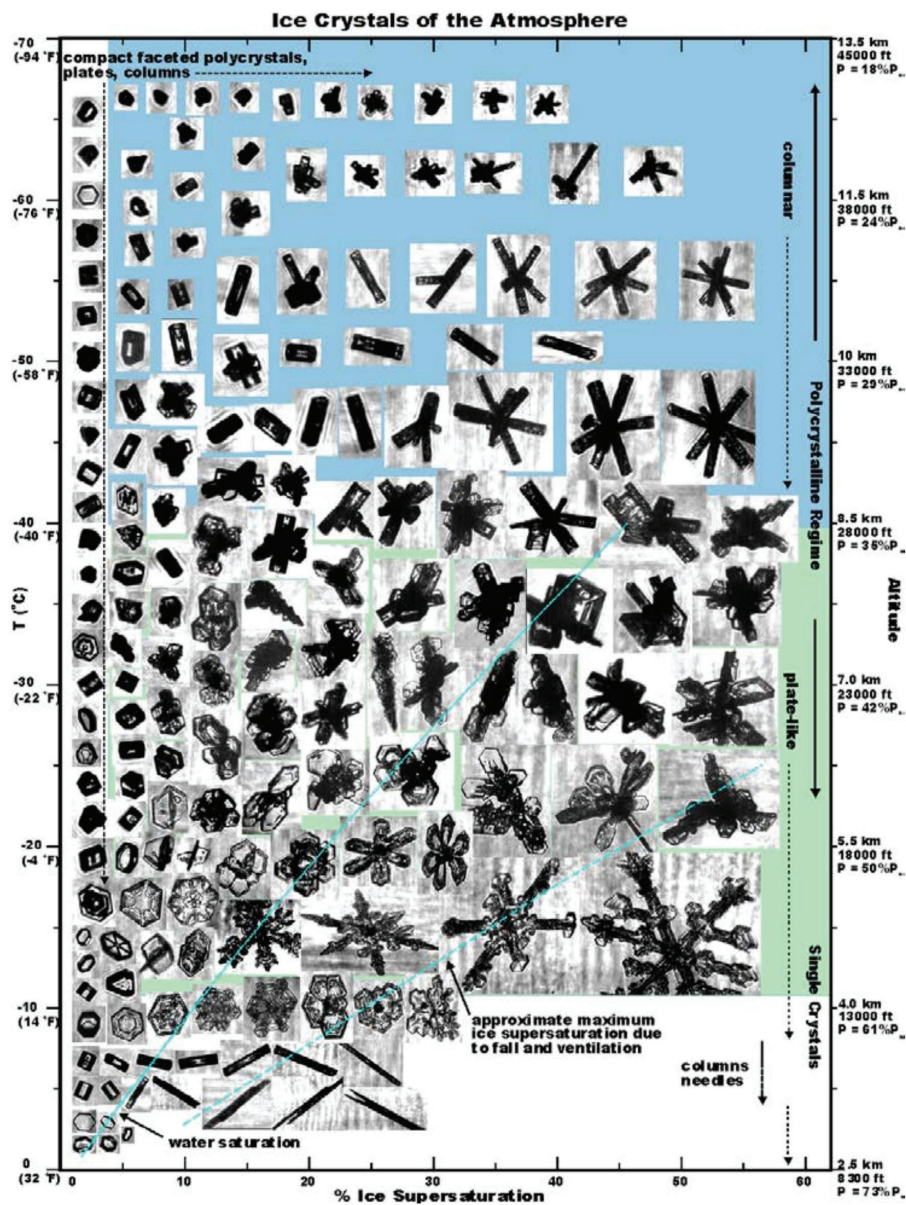


Figure 3.2: Diagram of ice crystal types derived from laboratory results and CPI images obtained during AIRS II and other field studies. The right axis gives approximate height and pressure of ice crystal formation, where P_0 is the standard atmosphere pressure. The left axis gives temperature, and the x-axis gives the level of ice supersaturation. This figure is taken from Mitchell et al. (2011), where it was adapted from Fig. 5 of Bailey and Hallett (2009).

and supersaturation, observed ice crystals include columns, needles, plates, bullet rosettes (bullet columns connected at the tips), and the classical dendrite snowflakes.

At a given temperature the crystal complexity increases with supersaturation, from compact plates or columns, to dendrites or bullet rosettes. Furthermore, the diagram can be divided by temperature into regions where either plate- or column-like particles are formed. The dominant particle type changes back and forth several times from plates to columns, at temperatures of roughly -4 , -8 , and -40 °C (plates below

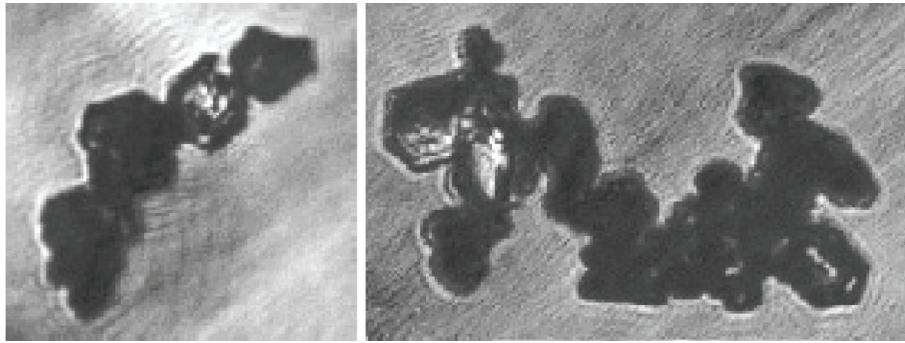


Figure 3.3: CPI images of hexagonal plate aggregates originating from an anvil cloud (Connolly et al., 2005). Images were taken using aircraft during the second Egrett Microphysics Experiment with Radiation Lidar and Dynamics (EMERALD-II) campaign. The lengths of the aggregates are 381 and 632 μm .

-4°C and columns above -40°C). There is also a division between single crystals and polycrystals at roughly -20°C , with mixed rosettes of plate-like components above -40°C and columnar rosettes below.

The ice particles in Fig. 3.2 are typical for ideal conditions where the temperature and humidity are approximately constant. In reality, an ice particle is subjected to a range of temperatures and humidities during its growth period. Typically, ice particles have been found to be defective and irregular in shape; perfect dendritic snowflakes are instead rarities.

3.3.3 Frozen precipitation

Ice hydrometeors do not grow towards large sizes through vapour diffusion alone; other processes are involved. Analogously to drop coalescence, large precipitating particles can be formed through *aggregation*, i.e., ice particles collide and aggregate to each other. Aggregation efficiency depends on temperature and ice particle shape. Dendritic crystals aggregate efficiently thanks to their branched shape, which allows them to interlock mechanically. Smoother ice crystals, such as columns and plates, can stick together due to electrostatic forces or surface melting, depending on temperature and relative humidity. Example images of plate aggregates are shown in Fig. 3.3. The interlocking aggregation is generally more effective than sticking. Aggregates formed by interlocking dendrites are found in Fig. 3.4.

Riming is another growth process important for frozen precipitation. Ice particles and snowflakes can grow by colliding with supercooled water droplets that freeze immediately upon contact, forming small, spherical ice structures on the surface. Figure 3.5 shows examples of rimed ice particles. As the degree of rime increases, the original particle becomes indiscernible, at which point it is referred to as *graupel*. Graupel takes on an either spherical or conical form, as seen in Fig. 3.5. The conical form is due the preferential orientation of the graupel, meaning that the droplets mainly hit and freeze at the bottom of the graupel. Riming occurs at temperatures down to about -40°C , i.e., at temperatures where supercooled water can exist. It is an overall important contributor to precipitation; instances where 30–50% of the

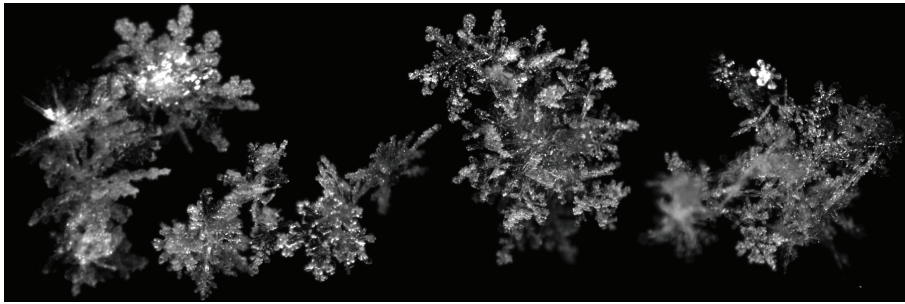


Figure 3.4: Example aggregates of dendrites. Images were taken using a MASC by Tim Garret, University of Utah (<http://www.inscc.utah.edu/~tgarrett/Snowflakes/Snowflakes.html>, accessed 11 Mars 2020).

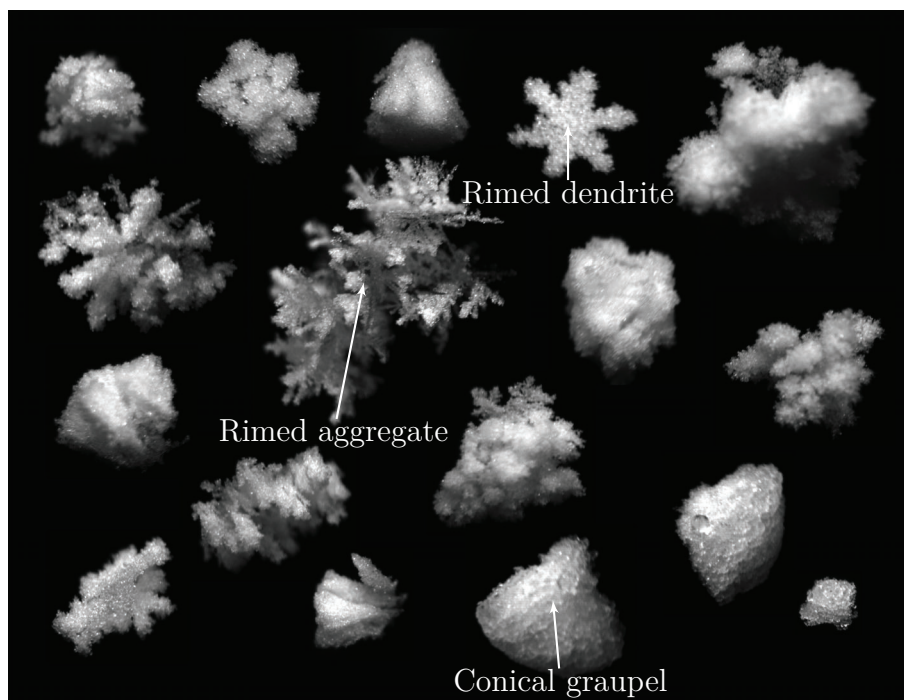


Figure 3.5: Example rimed particles. Several examples of conical graupel, a large rimed aggregate and a rimed dendrite can be seen. Images were taken using a MASC by Tim Garret, University of Utah (<http://www.inscc.utah.edu/~tgarrett/Snowflakes/Snowflakes.html>, accessed 5 Mars 2020).

total snowfall mass consisted of rime have been observed (Borys et al., 2003; Mitchell et al., 1990).

In certain extreme conditions, such as vigorous convective clouds with high liquid water content, riming can take the extreme form of hailstones. Hailstones up to 1 kg have been observed. As the hail particle falls through the cloud, it is bombarded with supercooled droplets at a high rate. The latent heat released by freezing keeps the hailstone at a temperature close to zero and collected droplets are thus prevented from freezing immediately, forming a wet surface on the hail. The liquid water either freezes slowly or is retained in internal cavities (Latham, 1969). Since the hail can be transported by up- and down-drafts several times, it may grow for a long time,

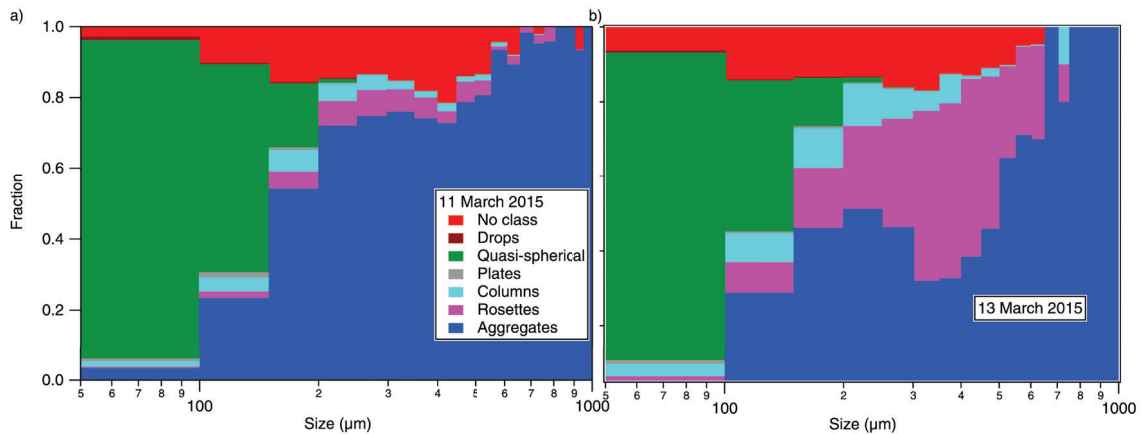


Figure 3.6: Ice particle type fractions as a function of particle size of two cirrus that were sampled during two separate flights. a) A developing cirrus cloud. b) A decaying cirrus cloud. Figure is taken from O’Shea et al. (2016).

until the strength of the up-draft can no longer support the hailstone mass. This also results in a layered structure of the hailstone.

3.4 Frequency of observed ice particle types

The previous section discussed the possible routes of ice particle growth given various conditions. Since the amount and global coverage of in-situ observations are limited, it is difficult to obtain accurate statistics on the frequency of a given particle type. Some key observations are nonetheless prevalent. Particles considered to be irregular (i.e., non-faceted single crystals) tend to dominate. Often, about 90 % of observed particles at lower sizes are found to be irregular (May et al., 2008; Um and McFarquhar, 2009; Zhang et al., 2013; O’Shea et al., 2016). This seemingly contradicts the diagram in Fig. 3.2. However, those particles were imaged in ideal conditions, which are generally not found in nature. As an example, Fig. 3.6 presents particle type fractions of airborne observations (O’Shea et al., 2016) for mid-latitude cirrus clouds, where irregular (quasi-spherical) particles are seen to dominate below 200 μm . Similar observations have been demonstrated for both tropical convective clouds and clouds in the Arctic, often with more than 90 % of observed particles being irregular (May et al., 2008; Um and McFarquhar, 2009; Korolev et al., 1999; McFarquhar et al., 2011). Exceptions exist; in certain conditions pristine crystals can dominate. For example, Orikasa et al. (2013) performed balloon measurements of mid-latitude cirrus and found that 45 % of observed particles were single bullets. Few of the observed particles were classified as irregular.

Figure 3.6 otherwise indicates that aggregates dominate at larger sizes, with rosettes claiming a large portion in the decaying cloud as well. The study by Baum et al. (2011) combined measurements from several field campaigns and saw a similar importance of aggregates for tropical deep convective ice clouds (anvil cirrus). The prevalence of aggregates at high altitudes is caused by the strong updrafts in deep convective cores, making it possible for large particles to exist at the top of the

clouds.

3.5 Particle characterisation

Before the particle size distribution is described, it is suitable with an overview of how particles are characterised in terms of size, mass, or shape. Defining the size of a particle is not always straightforward. A cloud droplet is essentially spherical and its size well-defined by its diameter. A larger rain drop is approximately spheroidal due to distortion by aerodynamic pressure and its shape is described by the major and minor axis. For frozen hydrometeors the situation is much more complicated. In special cases, such as with ice columns, the particle can be relatively well defined by its length and base diameter. In general, ice particles do not conform to simple geometric shapes, and there is a need for a more general way of parameterising particles. In addition, models also require simplified and general parameterisations. A set of parameters in use are described below.

The mass m is perhaps the most natural parameter for describing a particle and is also the most influential parameter regarding microwave scattering properties. For ice particles and rain drops, an alternative parameter commonly used is the mass equivalent sphere diameter

$$D_{\text{veq}} = \left(\frac{6m}{\pi\rho_i} \right)^{1/3}. \quad (3.2)$$

For ice particles, ρ_i is sometimes replaced by the liquid water density ρ_{lw} in which case D_{veq} can be viewed as the melted equivalent diameter (Petty and Huang, 2011). The mass or D_{veq} do not give any indication on the shape of the particle and is not the only particle parameter that influence electromagnetic scattering. Furthermore, in the case of in-situ measurements based on 2D-images (see Sec. 3.1), the mass is not easily retrieved since the full volume of the particles can not be directly measured.

The maximum dimension or diameter, D_{max} , is another parameter commonly used, more easily retrieved from 2D-images. In principle, it gives a measure on the spatial extent of the particle. However, there is much ambiguity in the remote sensing and in-situ community in how this parameter is defined. The definition is mostly influenced by the nature of the given study or instrument, and it is often unclear what exact definition that is actually used. In the case of in-situ 2D-imagery, the maximum dimension is usually defined as the maximum length found between two pixels of the image. This definition is heavily dependent on the particle orientation during the image capture, resulting in a bias towards lower values since the true maximum dimension is unlikely to be aligned with respect to the imager. Particle modellers can avoid this issue, either defining the maximum dimension as the maximum length between two surface points or as the diameter of the minimum circumscribing sphere (in which case maximum diameter is a more proper term). Many studies define D_{max} of hexagonal columns or plates by the length or face diameter, respectively. Such definitions can not be generalised to arbitrary shapes such as aggregates. Regardless, it should hold that $D_{\text{veq}} \leq D_{\text{max}}$, with equality only for spheres.

The relationship between mass and D_{\max} depends on the exact shape and can not be specified by a single expression. However, the general behaviour of the mass for a given particle type can often be approximated by a mass-size relationship, which relates particle mass and maximum diameter through a power-law as

$$m = \alpha D_{\max}^{\beta}, \quad (3.3)$$

where α and β are coefficients. The β -coefficient describes how the particle is growing with size, while α describes how dense or porous the particle is. Solid spheres have $\beta = 3$, plates that only grow along their edges have $\beta = 2$, and needles only growing along the major axis have $\beta = 1$. For aggregates, β has been found to be normally close to 2. Westbrook et al. (2004) provided a theoretical argument for why this should be the case. Columns and plates are usually observed having $\beta \approx 2.5$ (Auer and Veal, 1970; Mitchell and Arnott, 1994; Um et al., 2015).

Sometimes the aspect ratio (AR) (alternatively, axial ratio) is used to provide a measure of the non-sphericity of a particle. To some extent, AR influences the particle orientation (see Sec. 3.7). However, it is difficult to express geometrical properties of three-dimensional (often irregular) structures by a two-number ratio. Aspect ratio is therefore an inherently ambiguous and not clearly defined parameter, often defined differently by different authors. It is often taken as the ratio between the maximum dimension and the dimension in a perpendicular direction. Cloud crystals below $D_{\max} = 1$ mm demonstrate a large spread in aspect ratios, ranging from 1 to over 6 depending on crystal type (Um et al., 2015; Korolev and Isaac, 2003). Snowflakes or aggregates tend to have a median aspect ratio in between 1.5 and 2, while the aspect ratio of hail is close to 1 (Garrett et al., 2015). Riming shifts aspect ratio towards unity, since to the particle acquires an increasingly spherical shape.

In radiate transfer, the *size parameter* x is of importance. It describes the particle size compared to the wavelength of the radiation in question. It is defined as

$$x = \pi D / \lambda, \quad (3.4)$$

where λ is the wavelength and D the diameter (could be D_{veq} or D_{\max}). The size parameter is important because the general behaviour of electromagnetic interaction of particles depends on this variable. As will be discussed in Sec. 4.2, it is common to make the distinction between cases where $x \ll 1$, $x \approx 1$, or $x \gg 1$, referred to as the Rayleigh, Mie, and geometric optics regimes, respectively.

3.6 The particle size distribution

The particle size distribution (PSD) $\frac{\partial N}{\partial D}$ was already introduced in Sec. 2.4.2, defined as the number of particles per unit volume per unit particle size. In the remainder of this text, n is used to denote the PSD. It is of vital importance in radiative transfer modelling. Though not the main subject of this thesis, it is arguably as or more important than the shape of the particles.

Firstly, the number density N is found through integration of the PSD. If the volume equivalent diameter D_{veq} is used to describe the particle size, N is given by

$$N = \int_0^{\infty} n(D_{\text{veq}}) dD_{\text{veq}}. \quad (3.5)$$

The ice water content (IWC) is similarly described by

$$\text{IWC} = \int_0^{\infty} n(D_{\text{veq}})m(D_{\text{veq}}) dD_{\text{veq}} = \rho_i \frac{\pi}{6} \int_0^{\infty} n(D_{\text{veq}})D_{\text{veq}}^3 dD_{\text{veq}}. \quad (3.6)$$

Equivalent expressions hold for LWC or any other mass density parameter. Alternatively, if the PSD is expressed in D_{max} and the relationship in Eq. 3.3 is assumed,

$$\text{IWC} = \int_0^{\infty} n(D_{\text{max}})m(D_{\text{max}}) dD_{\text{max}} = \alpha \int_0^{\infty} n(D_{\text{max}})D_{\text{max}}^{\beta} dD_{\text{max}}. \quad (3.7)$$

To some degree it is possible to derive the PSD distributions from physical principles. However, in practice the number of processes and unknowns involved in determining the PSD means that in practice our current knowledge of PSDs stems from observations, mostly in-situ (see Sec. 3.1). In practical applications, size distributions are thus expressed using parameterisations or functional forms, where the modified-gamma distribution is the most common one (Petty and Huang, 2011). It is a four-parameter function described by

$$n(d) = N_0 d^{\mu} e^{-\Lambda d^{\gamma}}, \quad (3.8)$$

where d is some parameter describing the particle size and N_0 , μ , Λ , and γ are constants. Equation 3.8 is quite general. For instance, many distributions are described by a simple exponential, which Eq. 3.8 reduces to when $\mu = 0$ and $\gamma = 1$. The old Marshall-Palmer distribution for rain (Marshall and Palmer, 1948) is an exponential described by $N_0 = 8 \times 10^8 \text{ m}^{-4}$ and $\Lambda = 8200R^{-0.21} \text{ m}$. The exponential function implies that there is an increasingly high number of small particles, which is not realistic. However, the contribution of these small imaginary particles to the total mass content or any radiative property is in many cases negligible. This is often the case for rain and snow, where the larger hydrometeors contribute significantly more to the bulk properties than the smaller ones.

Example PSDs of ice hydrometeors are shown in Fig. 3.7, for one real measurement and two parameterisations. The MH97 parameterisation is from McFarquhar and Heymsfield (1997) and is based on aircraft measurements of anvil cirrus. The parameterisation from Field et al. (2007) is included using the mid-latitude setting denoted as F07m, mostly applicable to stratiform ice clouds. Also included are 2D-S measurements by the FAAM (Facility for Airborne Atmospheric Measurements) aircraft during the B895 flight (O'Shea et al., 2016). It corresponds to the bottom panel of Fig. 3.6. The IWC was estimated to $2.5 \times 10^{-4} \text{ g m}^{-3}$ and this value is as input to the MH97 and F07m PSDs. Furthermore, the cloud temperature was assumed to be 235 K.

The B895 data show a bi-modal distribution with a second peak at $170 \mu\text{m}$. Figure. 3.6 suggests that at approximately $200 \mu\text{m}$ almost 50% of the particles are

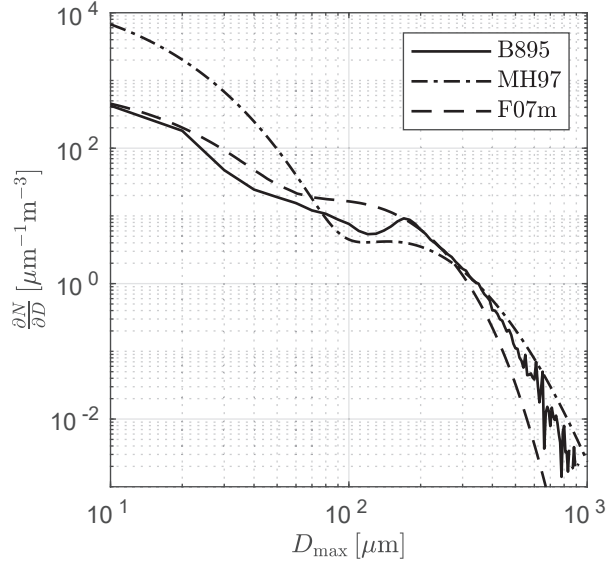


Figure 3.7: Example particle size distributions. Ice water content is assumed to be $2.5 \times 10^{-4} \text{ g m}^{-3}$.

aggregates, suggesting that the second peak is due to aggregates. The first mode is then composed quasi-spherical particles. However, it has been suggested that this mode is to a large degree composed of miss-sized, out-of-focus particles. As mentioned in Sec. 3.1, ice shattering can also lead to artefacts at small particle sizes. The parametrisations show similar tendencies as the B895 data, with particular good agreement for MH97 at sizes above 250 μm .

It should be clarified that comparing PSDs to each other has certain limitations, because assumptions on the physical properties of the particles are required. Since F07m and the B895 data are defined on D_{max} -grid, while MH97 is defined on D_{veq} -grid, conversion between these parameters is necessary. This is done using Eq. 3.2 and 3.3, giving

$$D_{\text{max}} = \left(\frac{\pi \rho_i D_{\text{veq}}^3}{6\alpha} \right)^{\frac{1}{\beta}}. \quad (3.9)$$

Hence, the α - and β -coefficients of the particles are required. In this case, β was set to 1.9 based on Brown and Francis (1995) and α was set to give consistent IWC using the B895 PSD, according to Eq. 3.7. Note that the F07m parameterisation uses α and β as input.

3.7 Particle orientation

For various applications it is important to not only consider the size and shape of a particle; its spatial orientation must be considered as well. The orientation refers to how the particle is spatially aligned with respect to the local zenith and azimuth reference, and is mainly influenced by the aerodynamic force acting upon the particle. Orientation is therefore coupled to the terminal velocity of the particle.

It can also influence the shape of the particle, such as for conical graupels. In some cases, orientation is important for the radiative properties of the particle.

A spherical liquid droplet effectively only has one orientation state due to its spherical symmetry. Ice particles on the other hand, are generally not spherical and can in certain conditions have a preferred orientation. Several studies have shown that polarisation signals in passive microwave and sub-millimetre measurements emerge from particles with a preferred orientation (Troitsky et al., 2003; Buehler et al., 2012; Xie et al., 2012; Defer et al., 2014; Gong and Wu, 2017). Oriented particles can be found in stratiform clouds and in convective clouds outside of the convective core where turbulence is relatively low, whereas ice particles in convective cores are more likely to be completely randomly oriented.

A thorough description of how the orientation state can be described is given in Paper D. To summarise, two main types of orientation are distinguished in this thesis. *Totally random orientation* (TRO) describes a completely isotropic distribution. Since the particle effectively becomes spherical, TRO is relatively simple to represent in modelling and is for many scenarios a valid assumption. A fluffy aggregate with an aspect ratio close to 1 is likely totally randomly oriented. Some particles are oriented with respect to the horizontal plane, i.e., particles that are non-spherical and experience aerodynamic drag. This state is labelled *azimuthally random orientation* (ARO). The particles are essentially allowed to rotate freely around the zenith axis, but are otherwise fixed in the plane with a constant tilt angle. Figure 3.8 illustrates the differences between TRO and ARO. Azimuthally random orientation is challenging to model in radiative transfer. Up until quite recently particles have generally been assumed to be TRO. Paper D and Lu et al. (2016) are the first attempts to remedy the situation for microwave frequencies.

Typically, the orientation of particles is described assuming an angular distribution function $p(\alpha, \beta, \gamma)$. The angles α , β , and γ are a set of angles describing the orientation of the particle. The Euler angles are one such set, which are assumed throughout this thesis and illustrated in Fig. 3.9. Orientation averaged properties can then be calculated through integration over all possible angles. For instance, the scattering matrix \mathbf{Z} (see Sec. 4.2) is orientation averaged according to

$$\mathbf{Z}_{\text{avg}}(\theta_i, \phi_i, \theta_s, \phi_s) = \int_0^{2\pi} \int_0^\pi \int_0^{2\pi} p(\alpha, \beta, \gamma) \mathbf{Z}(\theta_i, \phi_i, \theta_s, \phi_s, \alpha, \beta, \gamma) \sin\beta \, d\alpha \, d\beta \, d\gamma, \quad (3.10)$$

where θ_i is the incidence polar angle, ϕ_i the incidence azimuth angle, θ_s the scattering polar angle and ϕ_s the scattering azimuth angle. Note that the above expression is only valid for incoherent radiation, which is usually the case for atmospheric scattering and emission.

3.8 Shape data

As outlined in Sec. 1.2, the calculation of single scattering properties (SSP) requires a model of the particle shape. Considering the extreme variability of ice particles in nature, it is not straight-forward to represent the particle shape; several approaches

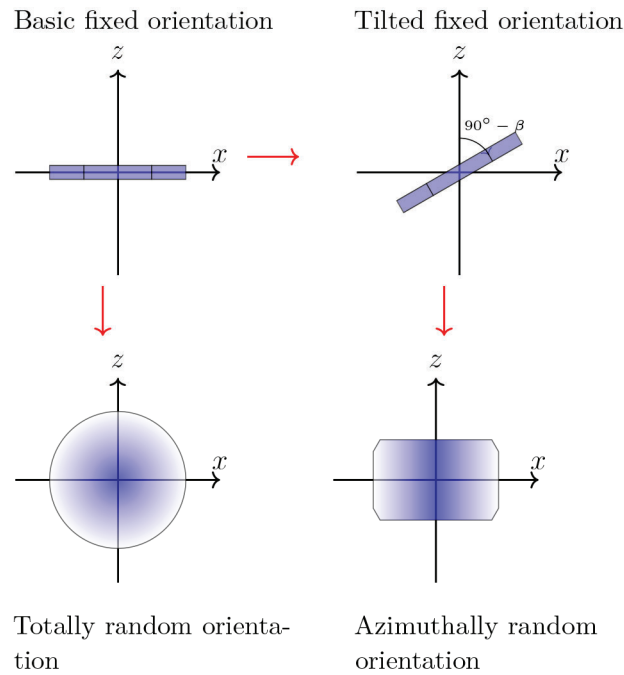


Figure 3.8: A schematic illustration of the difference between totally random (TRO) and azimuthally random orientation (ARO). (Top left) The particle in a fixed state, assumed to be a hexagonal plate (here seen from the side). (Bottom left) The particle in totally random orientation, effectively spherical with decreasing density outwards. (Top right) The particle in a fixed state, but with a tilt angle β applied. (Bottom Left) Azimuthally random orientation, i.e., rotation around the z-axis and the particle axis. The particle is effectively symmetric in the horizontal plane.

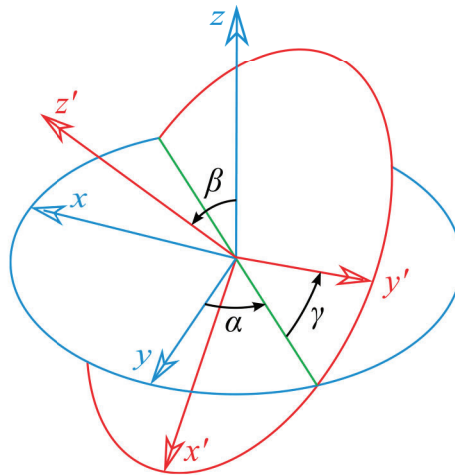


Figure 3.9: The Euler angles. Drawing is taken from Yurkin and Hoekstra (2014) and slightly modified.

exist. Figure 3.10 shows examples of idealised particle models in use in currently existing SSP databases. Particle models are often labelled as habits. Typically, the particle model is realised over a range sizes, following some sort of parameterisation such as the mass-size relationship in Eq. 3.3.

Ice particles have historically been modelled as spheroids or even spheres, since the computation of SSP of such particles is inexpensive (see Sec. 4.2.1). In order to model the “fluffiness” of aggregates, the dielectric properties (see Sec. 4.1) for the spheroids were modelled assuming an air-ice mixture, for instance using the Maxwell–Garnett mixing formula (Garnett, 1904). Such representations can give good results at single-frequency radiative transfer applications, since it is possible to tune the spheroid properties to match reference data. This approach has been shown to give poor results for multi-frequency applications (Geer and Baordo, 2014), hence the recent movement to more realistic representations of ice particles.

The early SSP databases considered idealised crystals. For instance, the sector snowflake from the SSP database by Liu (2008) is composed of three ellipsoids with a shared center. Its dimensions follow a parameterisation based on in-situ measurements of aggregates (Heymsfield et al., 2002; Heymsfield and Miloshevich, 2003) and consequently have a value of β equal to 1.44. This means that at small sizes it is spherical, while at large sizes it becomes thinner and thinner. The bullet rosette in Fig. 3.10, taken from the database by Hong et al. (2009), is another example of an idealised representation based on in-situ measurements. It has a β value equal to 2.42, meaning that the arms become increasingly thin (relatively to D_{\max}) as the size increase.

An alternative approach is to explicitly simulate the processes involved in the formation of the particles. For the database by Kuo et al. (2016), pristine crystals were modelled using a computational algorithm developed by Gravner and Griffeath (2009) that explicitly simulates snowflake growth. By varying supersaturation, initial crystal seed, etc., crystals similar to observations can be produced. Figure 3.11 shows examples of dendritic crystals generated using this method.

Aggregation can also be modelled, to various degrees of complexity. The aggregate in Fig. 3.10 is an idealised representation, where a fixed number hexagonal crystals of different sizes have been stuck together in a random fashion. The aggregate shape was then scaled to give a range of sizes, resulting in a value of β equal to 3, an unrealistic assumption for aggregates (should rather be close to 2 as discussed in Sec. 3.5). More recent studies attempt to model the aggregation more accurately. The database by Kuo et al. (2016) also includes aggregates of the generated pristine crystals, as shown in Fig. 3.11.

For the SSP data produced in paper A and B, the so called snowflake-toolkit (Rathsman, 2016) was developed and used to generate realistic aggregates. Using crystal shapes as input, aggregation is simulated using a semi-physical model. The model could be considered to describe a small section of a cloud with a number of ice particles in it. A number of events can happen at each iteration, being the aggregation of two particles, growth of a new crystal, particle melting, or particle fallout from the cloud. The likelihood of these events depends on a number of factors such as size, estimated fall speed, and a number of control parameters. Contrary to many other aggregate models used in the field, this model allows for the aggregation of two aggregates. The aggregate sticking occurs at the faces of the particles, and there are also control mechanisms to ensure that the building blocks of the aggregate does not overlap with each other. Aggregation occurs at randomly selected angles

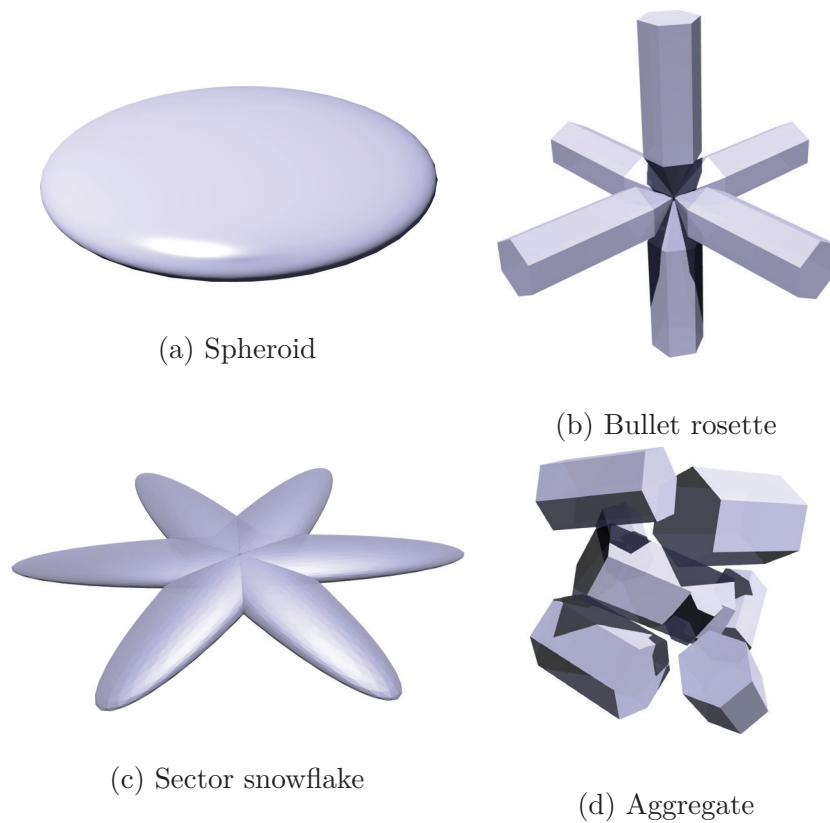


Figure 3.10: Example ice crystal shapes. a) Spheroid. b) Bullet rosette. c) Sector snowflake from the database by Liu (2008). d) Aggregate, originally described by Yang and Liou (1998). It was used in the databases of Hong et al. (2009) and Ding et al. (2017). Figures are rendered using the Blender software.

and orientations. If an aggregation event does not result in an accepted aggregate, it is discarded. Example images of generated aggregates are found on the cover of this thesis.

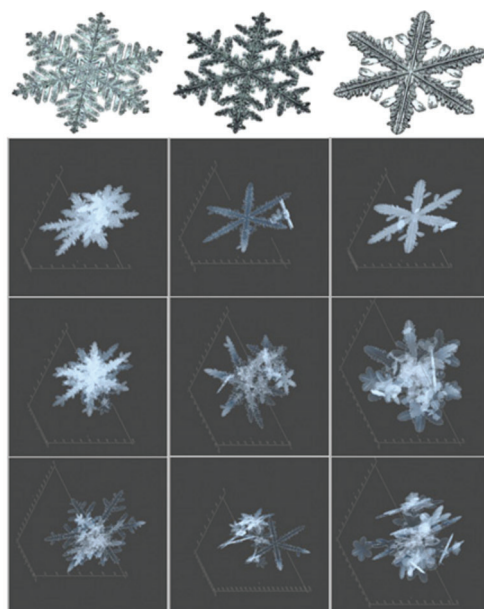


Figure 3.11: Examples of crystals and aggregates generated for the database by Kuo et al. (2016).

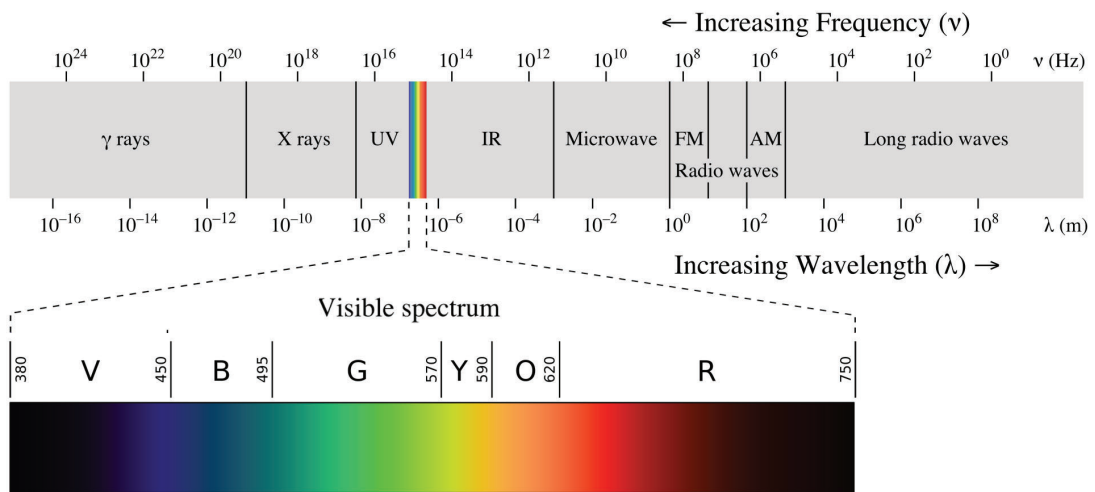


Figure 4.1: The electromagnetic spectrum. Image taken from Wikipedia commons (https://commons.wikimedia.org/wiki/File:EM_spectrumrevised.png, accessed 3 Mars 2020).

Chapter 4

Atmospheric radiative transfer

It is through electromagnetic radiation that Earth is warmed by the Sun and cooled through emission. Since the radiation interacts with the medium it passes through, one can also perform remote sensing of the atmosphere and gain important knowledge of its various components. These processes are described by atmospheric radiative transfer (RT). The most important parameters to consider are the wavelength λ or frequency ν , which are related to each other by

$$\lambda = \frac{c}{\nu}, \quad (4.1)$$

where c is the speed of light. Figure 4.1 gives an overview of the electromagnetic spectrum and highlights the different frequency bands. Depending upon the wavelength, the relevant physical processes and measurement principles differ greatly.

Having discussed the microphysics and the role of hydrometeors in the atmosphere in previous chapters, this chapter now turns to their interaction with electromagnetic radiation. The focus is towards remote sensing in the microwave band, but for completeness sake infrared (IR) and visible light are discussed as well, which are the most important bands for Earth's radiative budget.

4.1 Electromagnetic wave propagation

Radiation can be understood as electromagnetic waves that propagate at the speed of light c as described by Maxwell's equations. For a given frequency ν , electromagnetic radiation is characterised by three other properties: the phase ϕ , intensity I , and the polarisation. It is through these basic properties that information can be retrieved through remote sensing. Depending on the measurement technique and the frequency region, different properties are taken advantage of in remote sensing.

Radiation in the form of monochromatic (single wavelength radiation) electromagnetic waves, propagating along the z -direction, is described by the complex valued electric field vector (in units of V m^{-1}), which in vector form is given by

$$\vec{E} = \begin{pmatrix} E_v \\ E_h \end{pmatrix} = \begin{pmatrix} E_{v0}e^{-i\phi_v} \\ E_{h0}e^{-i\phi_h} \end{pmatrix} e^{-i(\omega t - kz)}. \quad (4.2)$$

The polarisation describes the geometric orientation of \vec{E} and how it varies with time. Here, v and h denote the horizontal and vertical polarisation, which are aligned along the y - and x -axis, respectively. The polarisation state is determined by the relative magnitudes of E_{v0} and E_{h0} and the phase difference $\Delta\phi = \phi_h - \phi_v$. Otherwise, t is the time, ω is the angular frequency, and k is the wavenumber. ω is related to the cyclic frequency ν as $\omega = 2\pi\nu$ and k to the wavelength as $k = \frac{2\pi}{\lambda}$. Radiation is also described by the magnetic field vector \vec{B} , which is perpendicular to \vec{E} . It can be described similarly to Eq. 4.2, but is omitted in the rest of this thesis, since it is uniquely determined by \vec{E} .

In general, remote sensing instruments do not measure the complex electric field vector, but the flux density F in units of W m^{-2} . In other words, F is the radiant energy passing through a unit area per second. It can be defined as

$$F = \frac{dP}{dA}, \quad (4.3)$$

where dP is the radiant energy passing through a unit area dA per second. In the case of a monochromatic electric field as previously described, F is given by

$$F = \frac{1}{2} \sqrt{\frac{\mu_0}{\epsilon_0}} [\langle E_v E_v^* \rangle + \langle E_h E_h^* \rangle] = \frac{1}{2} \sqrt{\frac{\mu_0}{\epsilon_0}} [E_{v0}^2 + E_{h0}^2], \quad (4.4)$$

where the brackets indicate time-averages.

It is assumed that the electric field is propagating through a medium which can be described by its refractive index $n = \sqrt{\epsilon_r \mu_r}$, where ϵ_r is the relative permittivity and

μ_r the relative permeability of the medium¹. The constants ϵ_r and μ_r are measures of a medium's response to an external electric and magnetic field, respectively, and they can both take on complex values. Consequently, n can be complex-valued as well. The wavenumber k is related to n by $k = \frac{\omega n}{c} = \frac{\omega}{c} \sqrt{\epsilon_r \mu_r}$. Note that the speed of light in vacuum is $c = 1/\sqrt{\epsilon_0 \mu_0}$, where ϵ_0 and μ_0 are the permittivity and permeability of vacuum, while the phase speed in a particular medium is $v = c/\sqrt{\epsilon_r \mu_r}$.

Radiation in the atmosphere is not monochromatic, it consists of a range of wavelengths. Also, the radiation typically has an angular distribution. F covers the total power P of the radiation received from all directions of the half-sphere above dA and at all wavelengths. An alternative parameter is the *spectral radiance* L_λ , which describes the flux density within a unit solid angle $d\Omega$, a measure of the field of view, and the wavelength interval $[\lambda, \lambda + d\lambda)$. It is defined by

$$L_\lambda = \frac{dP}{d\Omega dA d\lambda} \quad (4.5)$$

and has units² of $\text{W sr}^{-1} \text{m}^{-2} \text{m}^{-1}$. It is important to note that dA is the unit area normal to the propagation direction. The radiance is in certain cases more suitable than the flux density, for instance when scattering needs to be considered and angular direction is important.

4.1.1 Attenuation

An electric field travelling through a homogeneous medium with a complex-valued refractive index $n = n_r + in_i$ will experience attenuation, which can be understood as follows. The wavenumber is $k = k_r + ik_i = (n_r + in_i)\frac{\omega}{c}$ and it follows that E_v in Eq. (4.2) can be written as

$$E_v = E_{v0} e^{-\frac{n_i \omega}{c} z} e^{-i(\omega t - k_r z - \phi_v)}. \quad (4.6)$$

An attenuating exponential that depends on n_i has been introduced. The flux density for vertically component of the electric field can then be written as

$$F_v = \frac{1}{2} \sqrt{\frac{\mu_0}{\epsilon_0}} E_{v0}^2 e^{-\frac{z}{l_a}}, \quad (4.7)$$

where $l_a = \frac{c}{2\omega n_i}$ is the *absorption length*, defined as the distance where the flux density has been attenuated by a factor e^{-1} .

Refractive indices of both frozen and liquid water vary strongly with frequency and exhibit a significant temperature dependence at microwave wavelengths. In Fig 4.2, l_a is plotted as a function of frequency at selected temperatures in the case of ice and liquid water. At visible frequencies above 400 THz, l_a is very long

¹It is here assumed that the refractive index does not depend on the polarisation, i.e., the material is not *birefringent*. Furthermore, we only consider non-magnetic materials which have $\mu_r = 1$. For the applications considered in this thesis, these are reasonable assumptions.

² The spectral radiance can just as well be given in terms of frequency, i.e., $L_\nu = \frac{dP}{d\Omega dA d\nu}$ in units of $\text{W sr}^{-1} \text{m}^{-2} \text{Hz}^{-1}$.

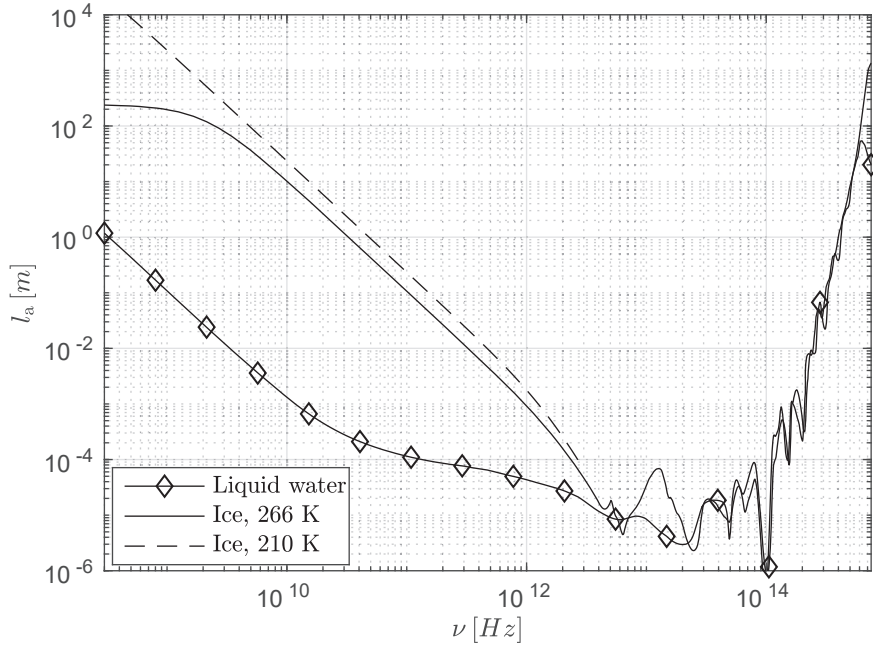


Figure 4.2: Absorption length as a function of frequency ν . The refractive indices of ice at 210 K and 266 K are computed based on parametrisations given by Mätzler (2006) and Warren and Brandt, 2008, respectively. The refractive index of liquid water is calculated using Segestein (1981). It is unclear at what temperature the liquid water refractive index parameterisation is valid for. A comparison to the parametrisation by Ellison (2007) at microwave frequencies indicates 300 K.

for both frozen and liquid water, up to 900 and 50 m, respectively. This explains the transparency of ice and water at visible light. At microwave frequencies, below 300 GHz the picture is different. At 100 GHz, l_a is 10 m for ice, being relatively transparent. In contrast, water is strongly absorbing, with $l_a \approx 1$ mm at 100 GHz. This explains why microwave ovens, which operate at around 2.5 GHz, have a hard time heating up frozen food compared to already unfrozen food. Figure 4.2 also shows that at infrared frequencies, l_a is very short (less than 0.1 mm) for both ice and liquid water. This has implications for the role of clouds in Earth's radiative budget (see Sec. 2.6), which will be further described in Sec. 4.6.2.

4.1.2 Stokes vector

A common way to describe the flux density and polarisation is through the Stokes vector (Stokes, 1851; Mishchenko et al., 2002)

$$\mathbf{I} = \begin{bmatrix} S_0 \\ S_1 \\ S_2 \\ S_3 \end{bmatrix} = \frac{1}{2} \sqrt{\frac{\mu_0}{\epsilon_0}} \begin{bmatrix} \langle E_v E_v^* \rangle + \langle E_h E_h^* \rangle \\ \langle E_v E_v^* \rangle - \langle E_h E_h^* \rangle \\ \langle E_v E_h^* \rangle + \langle E_h E_v^* \rangle \\ i (\langle E_h E_v^* \rangle - \langle E_v E_h^* \rangle) \end{bmatrix} = \frac{1}{2} \sqrt{\frac{\mu_0}{\epsilon_0}} \begin{bmatrix} \langle E_{v0}^2 \rangle + \langle E_{h0}^2 \rangle \\ \langle E_{v0}^2 \rangle - \langle E_{h0}^2 \rangle \\ \langle 2E_{v0} E_{h0} \cos(\Delta\phi) \rangle \\ \langle 2E_{v0} E_{h0} \sin(\Delta\phi) \rangle \end{bmatrix}, \quad (4.8)$$

where S_0 is equal to the total flux density. \mathbf{I} can be normalised to have the same unit as the spectral radiance if needed. The remaining elements describe the polarisation state. In short, S_1 and S_2 describe linear polarisation and S_3 describes the circular

polarisation. The Stokes vector has the convenient property that two incoherent waves (randomly changing phase difference and thus polarisation) can be added or decomposed linearly. Radiation in nature is generally incoherent and contains a range of frequencies. In the atmosphere, particles are positioned in a random fashion, i.e., scattered and emitted light will have random phase and different frequencies.

4.2 Scattering and absorption by particles

Single scattering properties (SSP) describe the scattering, absorption, and emission of incident radiation by single particles (molecules, aerosols, and hydrometeors). It is the main topic of this thesis and of fundamental importance for atmospheric RT. For an incident electric field the SSP of a particle is fully described by the complex scattering amplitude matrix \mathbf{S} (size 2×2) in units of m^{-1} . It relates the incident and outgoing field as

$$\begin{bmatrix} E_v(r, \hat{\mathbf{n}}') \\ E_h(r, \hat{\mathbf{n}}') \end{bmatrix} = \frac{e^{-ikr}}{r} \mathbf{S}(\hat{\mathbf{n}}', \hat{\mathbf{n}}) \begin{bmatrix} E_v(0, \hat{\mathbf{n}}) \\ E_h(0, \hat{\mathbf{n}}) \end{bmatrix}, \quad (4.9)$$

where r is the distance to the particle, and $\hat{\mathbf{n}}'$ and $\hat{\mathbf{n}}$ the propagation vectors of the scattered field and incident fields, respectively (Mishchenko et al., 2002). While this relationship is compact and general, radiation is typically not described using the electric fields in atmospheric RT. In terms of the Stokes vector \mathbf{I} (Eq. 4.8), the angular distribution of scattered radiation is

$$\begin{bmatrix} S_0(r, \hat{\mathbf{n}}') \\ S_1(r, \hat{\mathbf{n}}') \\ S_2(r, \hat{\mathbf{n}}') \\ S_3(r, \hat{\mathbf{n}}') \end{bmatrix} = \frac{\mathbf{Z}(\hat{\mathbf{n}}', \hat{\mathbf{n}})}{r^2} \begin{bmatrix} S_0(r, \hat{\mathbf{n}}) \\ S_1(r, \hat{\mathbf{n}}) \\ S_2(r, \hat{\mathbf{n}}) \\ S_3(r, \hat{\mathbf{n}}) \end{bmatrix}. \quad (4.10)$$

where \mathbf{Z} (in units of m^2) is the four-by-four scattering matrix³ which can be derived from \mathbf{S} . Note that the equation describes scattered radiation in the far field, i.e., at r much greater than the particle size. In contrast to \mathbf{S} , \mathbf{Z} does not uniquely characterise the SSP; one additional parameter is required.

In the simple scenario that only the total radiance is considered, the fraction of energy scattered by the particle is described through the scattering cross-section σ_s , a scalar with units of m^2 . It is given by integration over the solid angle⁴

$$\sigma_s = \int_{4\pi} \mathbf{Z}_{11} d\hat{\mathbf{n}}', \quad (4.11)$$

Given incident radiation with flux density S_0 , the scattered power is then equal to $\sigma_s S_0$. Similarly, the energy absorbed by the particle is determined by σ_a . It is typically convenient to consider the effect of absorption and scattering simultaneously,

³ \mathbf{Z} is frequently denoted as the phase matrix, but the scattering matrix (e.g. Bohren and Battan, 1980) is a more descriptive name.

⁴Multiple other normalisations of \mathbf{Z} are in use, in which case some factor in front the integrand is required for the calculation of σ_s .

i.e., the total attenuation of the radiation. It is described by the extinction cross section as

$$\sigma_e = \sigma_a + \sigma_s. \quad (4.12)$$

When considering the full polarisation state using the Stokes vector, extinction can be characterised by the 4-by-4 extinction matrix \mathbf{K} (in units of m^2). It is essentially a generalisation of σ_e that describes the attenuation of all Stokes elements. \mathbf{K} is calculated by evaluating \mathbf{S} in the forward direction, and σ_e is equal to \mathbf{K}_{11} . The matrices \mathbf{Z} and \mathbf{K} describe the SSP completely, because the absorption is just the difference between the two.

The nature of particle absorption and scattering depends on various factors for which different physics must be applied. Absorption by gases is described by quantum mechanics. Atoms absorb and emit radiation at discrete energy levels corresponding to electron orbits. Molecules also possess vibrational and rotational energy states, depending on the structure of the molecule. In an absorption spectrum, these energy states correspond to absorption lines at which the gas absorbs and emits. The absorption lines have a finite width due to a number of line broadening processes. Natural broadening is due to the finite lifetime of the given excited state and the inherent uncertainty in energy. However, in the atmosphere other broadening processes are more important. Doppler broadening is due to the Doppler shifts caused by the distribution of the molecule velocities and is mostly important at altitudes above 60 km. Pressure broadening dominates in troposphere, and is due to molecule collisions that reduce the lifetimes of the excited states and consequently increase the uncertainty in energy.

Macroscopic particles such as aerosols are composed of multiple molecules whose energy levels overlap with each other, creating a continuous absorption spectrum. Macroscopic particles can thus be treated according to electromagnetic theory. Different theoretical frameworks must be applied to particles of different sizes, mainly determined by the size parameter x (see Eq. 3.4). The refractive index and shape of the particle are also important. When the particle is small compared to the wavelength, i.e., $x \ll 1$, scattering can be derived by considering the particle as a single electric dipole. The incident electric field can be considered to be roughly spatially constant over the domain of the particle. This regime is commonly referred to as the *Rayleigh* regime, and the dependence on shape is relatively low. In Fig. 4.3, calculated extinction, scattering, and absorption efficiencies Q are plotted against x , assuming an ice sphere at 439 GHz. The efficiencies are unitless and defined as the cross section divided by the cross-sectional area of a volume equivalent sphere, i.e.,

$$Q = \frac{4\sigma}{\pi D_{\text{veq}}^2}. \quad (4.13)$$

As can be deduced from the figure, Q_a and Q_s are proportional to λ^{-1} and λ^{-4} , respectively, in the Rayleigh regime ($x < 1$).

It is also implied that ice particles in the Rayleigh regime should mostly absorb, i.e., they are relatively inefficient scatters and extinction is mostly due to absorption. This is can be described the *single scattering albedo* ω_0 , which describes the fraction

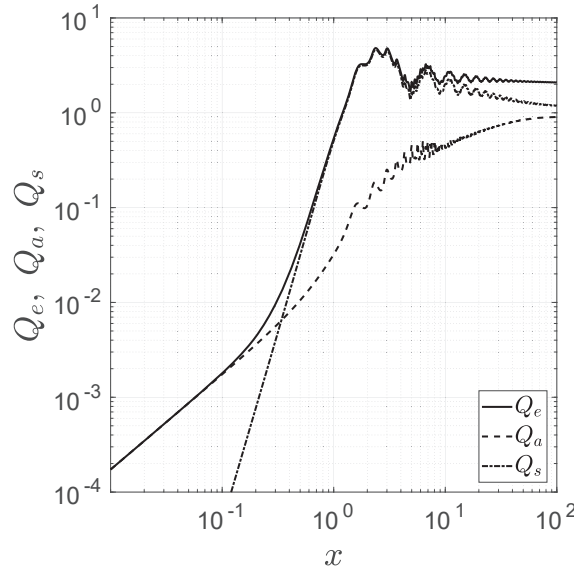


Figure 4.3: Extinction, scattering, and absorption efficiency as a function of size parameter for an ice sphere. The refractive index is set to $n_{ice} = 1.78 + 0.011i$.

of the incident radiation that is scattered compared to the total attenuation. It is defined as

$$\omega_0 = \frac{\sigma_s}{\sigma_e}. \quad (4.14)$$

Purely scattering particles have a single scattering albedo of 1.0, while $\omega_0 = 0.0$ indicates a purely absorbing particles. In Fig. 4.3, ω_0 goes from a low value to roughly 0.6 for large x . For other particles, this may not be the case, depending on their dielectric properties. For example, solar radiation at visible wavelengths experience little absorption by air molecules (due to lack of absorption lines at these frequencies) and is mostly affected by Rayleigh scattering, causing the blue color of the sky. Due to the λ^{-4} -dependence of Rayleigh scattering, scattering of red wavelength (≈ 650 nm) is inefficient in comparison, but can be observed during sunsets when the path-length through the atmosphere is at its maximum (at which point the blue wavelength has been scattered away).

In Fig. 4.4, the angular distribution of radiation scattered by ice particles at various sizes, is shown. For $x = 0.01$ the distribution consists of two symmetrical forward and backward lobes of equal strength. A simplified measure of the angular scattering distribution is the *asymmetry parameter* g . It is a measure of the balance between forward ($\Theta < 90^\circ$) and backward scattering ($\Theta > 90^\circ$), where Θ is the scattering angle (see Fig. 4.4). The definition of g is

$$g = \frac{1}{\sigma_s} \int_{4\pi} \cos(\Theta) \mathbf{Z}_{11} d\hat{\mathbf{n}}'. \quad (4.15)$$

Isotropic scattering results in $g = 0$, while total back- or forward-scattering results in -1 or 1, respectively.

At size parameters $x \approx 1$, commonly referred to as the Mie regime, the single dipole argument is no longer applicable because the dipoles will no longer oscillate in

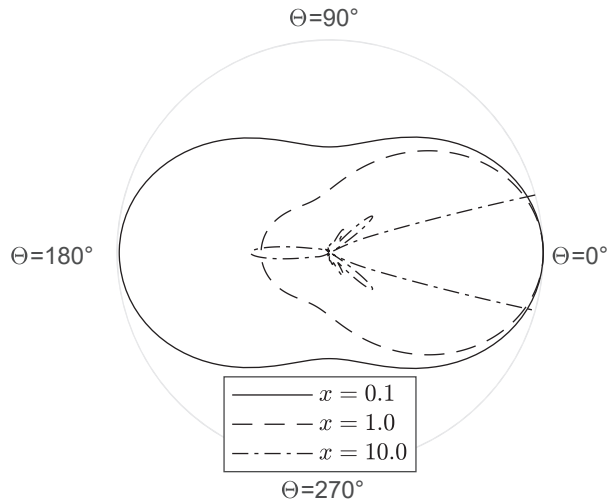


Figure 4.4: Angular distributions of \mathbf{Z}_{11} for ice spheres at three different size parameters (normalised to fit in the plot). The 0° angle is defined as the direction of the incident radiation. Note that only a small portion of the function for $x = 10$ is displayed, since the forward lobe is very large in comparison to the backward lobe. Mie theory was used to calculate \mathbf{Z}_{11} .

phase in response to an external electric field. At $x > 2$, Fig. 4.3 shows constructive and destructive interference of internally reflected fields in the particles. Q_e has also plateaued and converges towards a value of two, i.e., the extinction cross section is a factor 2 larger than the cross sectional area of the particle. A value of σ_e larger than 1 is possible due to diffraction, i.e., light is scattered around the edges of the sphere. Figure 4.4 shows that the angular distribution of the scattering increasingly favours forward scattering as x increases. The distribution is also more complex at $x = 10$, with side lobes visible.

When the size parameter is larger than 50, the scattering is considered to be in the geometric optics regime. At these large particle sizes, the scattering is calculated using optical methods such as ray tracing.

One should also mention the radar back-scattering coefficient, which gives the radiance that is scattered in the backward direction ($\hat{\mathbf{n}}' = -\hat{\mathbf{n}}$). The radar back-scattering coefficient (Mishchenko et al., 2002) is given by

$$\sigma_b = 4\pi\mathbf{Z}_{11}(-\hat{\mathbf{n}}, \hat{\mathbf{n}}). \quad (4.16)$$

Calculating the scattering properties of particles is in many cases a non-trivial problem, and is the main issue of paper A, B, D, and E. The next section 4.2.1 provides an overview of the methods that can handle this problem.

4.2.1 Techniques for calculating single scattering properties

Several methods to calculate the SSP of particles exist. As discussed in the previous section, the Rayleigh approximation can be used for small particles at long wavelengths. Alternatively, an analytic solution exists for homogeneous spherical particles according to Mie theory (Mie, 1908). Mie theory calculates the scattering

properties through separation of variables in spherical coordinates. The amplitude scattering matrix \mathbf{S} is obtained as infinite series of products of orthogonal basis functions (Mishchenko et al., 2002). The extinction and the scattering efficiencies are given by

$$Q_e = \frac{2}{x^2} \sum_{l=1}^{\infty} (2l+1)(|a_l^2| + |b_l^2|), \quad (4.17)$$

$$Q_s = \frac{2}{x^2} \sum_{l=1}^{\infty} (2l+1)\text{Re}(a_l + b_l), \quad (4.18)$$

where a_l and b_l are the Mie coefficients, which depend on the refractive index of the particle medium. The Mie equations are valid over all sizes and yield cross sections approximately equal to the Rayleigh scattering at small size parameters. Mie theory is in many cases a suitable approximation, such as for liquid droplets. However, ice particles are generally not spherical and their SSP deviate significantly from Mie theory at higher microwave frequencies. For such cases, numerical methods have to be employed. The choice of scattering method mostly depends on whether one is in the Mie or geometric optics regime. For ice particles at microwave and sub-millimetre wavelengths, most scattering occurs in the Mie regime.

The highly accurate T-matrix method involves calculating the so called T-matrix, which relates the expansion coefficients of the incident field to that of the scattered field (Waterman, 1965; Mishchenko et al., 1996). The advantage is that the T-matrix is not dependent on the incident radiation direction. Once the T-matrix is derived, scattering in any direction can be calculated analytically. The T-matrix can be calculated in a number of ways. For instance, Waterman (1965) used the Extended Boundary Condition Method (EBCM) that is based on solving the surface integral equations. It is suitable for symmetrical particles with smooth surfaces, like spheroids or cylinders. In general, the T-matrix method is an efficient option if the particle can be modelled in a simple fashion, especially if symmetries can be exploited (Kahnert, 2016). However, for complex morphologies the computational time increases significantly, and the applicable size parameter range may also turn out to be severely limited. In Paper E, the T-matrix method was used to calculate the SSP of non-spheroidal rain drops.

In later years, the Discrete Dipole Approximation (DDA) method (Draine and Flatau, 1994) has become the most common method for calculating scattering properties of complex ice particles at microwave frequencies. The idea is to approximate the particle by a grid of polarisable points, and solve the resulting equation system iteratively. The DDA equation for a grid of N dipoles is given by

$$\alpha_i^{-1} \mathbf{P}_i - \sum_{j \neq i}^N \bar{\mathbf{H}}_{ij} \mathbf{P}_j = \mathbf{E}_i^{inc}, \quad (4.19)$$

where \mathbf{P}_i is the dipole polarisation, \mathbf{H} the total interaction term and α_i the dipole polarisability. Once the dipole polarisation grid \mathbf{P} is known, any scattering parameter can be derived. The main advantage of DDA is that it treats arbitrary morphologies and is stable. However, DDA is computationally very demanding. The computation

time increase with the number of dipoles (equivalently, particle size or mass) and frequency. Particle shape and the refractive index also influence the computation time. Higher refractive index increases the computation times, which is luckily not a problem for ice but may be problematic for liquid or melting particles. In order to produce accurate results, the dipole grid must be fine enough to resolve the essential features of the particle. A common criteria used is

$$\frac{\pi|n|D_p}{\lambda} < t, \quad (4.20)$$

where D_p is the length of a single dipole and t is some constant that should not be larger than 0.25, giving a dpl (dipoles per wavelength) of approximately 22 for ice at microwave frequencies. In order to calculate orientation-averaged SSP, the DDA output must also be integrated over multiple orientation angles (or equivalently incidence angles). This further increase the computation time, because in contrast to the T-matrix method, DDA must be re-run for each required orientation angle (Kahnert, 2016). Despite its drawbacks, it is the most convenient method for arbitrarily shaped particles at microwave frequencies. It was therefore employed in paper A, B, and E for calculating the SSP of ice particles.

Other methods that bear mentioning are the Rayleigh-Gans theory (Leinonen et al., 2018) and The Generalised Multiple Mie (GMM) method (Xu, 1995). For scattering in the geometric optics regime, ray-tracing techniques must be used, such as the Improved Geometrics Optics Method (IGOM) (Yang and Liou, 1996).

4.3 Thermal radiation

All normal (baryonic) matter, regardless of phase, absorb and emit thermal radiation. The intensity and spectrum of thermal radiation are related to the temperature of the matter in question. The Sun is the main source of thermal energy on Earth. The solar radiation is consequently absorbed by the surface and atmosphere, heating Earth and driving Earth's weather. Conversely, Earth emits radiation out in space, which effectively cools it. These two processes are in equilibrium, meaning that Earth's mean temperature is maintained at a constant level over short time frames (short in a climatology point of view).

Thermal radiation essentially represents a conversion from the internal energy of the object to the emitted electromagnetic radiation. Typically thermal radiation is explained through the concept of a perfect black body. The black body is defined by the fact that it absorbs all incident radiation.

Black-body radiation is described by Planck's law, which gives the emitted spectral radiance $B_{\lambda,p}$ (p denotes Planck) in units of $\text{W m}^{-2} \text{sr}^{-1} \text{m}^{-1}$ as

$$B_{\lambda,p}(\lambda, T) = \frac{2hc^2}{\lambda^5 (e^{hc/\lambda k_B T} - 1)}, \quad (4.21)$$

where h is the Planck constant and k_B is the Boltzmann constant.

In Fig. 4.5, the Planck function is plotted at temperatures similar to the Sun and Earth, 6000 and 300 K, respectively. The functions have been normalised in terms

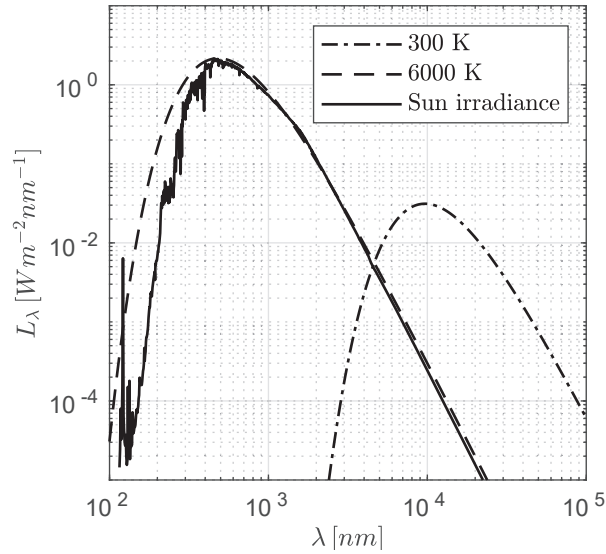


Figure 4.5: Planck's law in terms of wavelength for two temperatures, 300 and 600 K. Solar spectral irradiance is also included (Coddington et al., 2015)

of the solid angle, under the assumption that the observer is located at the top of Earth's atmosphere and the Sun is at zenith. The Sun spectral radiance is integrated over the solid angle of the Sun, and is denoted as the solar spectral irradiance with units of $\text{W m}^{-2} \text{m}^{-1}$. Earth spectral radiance is instead integrated over the half sphere on top of Earth's atmosphere, and is denoted as Earth spectral exitance (also in units of $\text{W m}^{-2} \text{m}^{-1}$). Essentially, the spectral irradiance and exitance here give a measure on the absorbed and emitted power of a square meter on the top of Earth's atmosphere. The 300 K curve peaks at roughly $9.64 \mu\text{m}$ (thermal infrared) while the 6000 K curve peaks at 482 nm (blue wavelength). At roughly $4 \mu\text{m}$ the solar spectral irradiance and Earth spectral exitance are approximately equal. This wavelength is therefore often taken as the limit between shortwave and longwave frequencies.

While the Sun is relatively well approximated by a black body, it is still only a theoretical concept. Real objects are to be considered as grey bodies, whose emitted radiation is described by

$$B_\lambda = \epsilon(\lambda)B_{\lambda,p}, \quad (4.22)$$

where ϵ is the emissivity of the material. Figure 4.5 shows the solar irradiance as measured at the top of Earth's atmosphere. Below 400 nm , the solar irradiance clearly deviates from the black-body spectrum. According to Kirchhoff's law of thermal radiation, the emissivity must be equal to the material's absorbance $a(\lambda)$, i.e., the fraction of light absorbed (not reflected) by the material. This assumption requires local thermal equilibrium (LTE), i.e., the medium is in thermodynamic equilibrium with its surroundings.

The same principle holds for macroscopic particles such as liquid drops and ice particles. A particle with absorption cross-section σ_a will emit with a radiant intensity ($\text{W sr}^{-1} \text{m}^{-1}$) equal to

$$B_\lambda = \sigma_a(\lambda)B_{\lambda,p}. \quad (4.23)$$

As seen in Fig. 4.3, a spherical ice particle is an inefficient emitter and absorber at low size parameters.

Using Taylor expansion of $e^{hc/\lambda k_B T}$, Eq. 4.21 can be approximated as

$$B_{\lambda,p}(\lambda, T) = \frac{2k_B T c^2}{\lambda^4}, \quad (4.24)$$

if $\frac{hc}{\lambda k_B T} \ll 1$. This is called the Rayleigh-Jeans approximation and corresponds to the curves to the right in Fig. 4.5. In passive microwave RT, the measured intensity is almost always expressed as the *brightness temperature* T_b , defined as the temperature of a pure black body that emits radiance of equivalent strength to that of the measured radiance. If the measured radiance is L_λ , then T_b is given by solving

$$L_\lambda = B_{\lambda,p}(\lambda, T_b). \quad (4.25)$$

Under the Rayleigh-Jeans approximation, the brightness temperature becomes directly related to the temperature as

$$T_b = \epsilon(\lambda)T. \quad (4.26)$$

This formula is very useful in microwave RT and gives an intuitive measure of the relationship between the object and the measurement.

4.4 The radiative transfer equation

It is now time to present the fundamental equation used to describe the propagation of electromagnetic radiation, the *radiative transfer equation* (RTE). It comes in many forms, depending upon the application and the degree of detail required to describe the phenomena involved. The most general form of the RTE that describes the interaction with electromagnetic radiation and atmospheric components (i.e., gases and particles) at LTE conditions and accounts for polarisation and multiple scattering, can be written as

$$\begin{aligned} \frac{d\mathbf{I}(\nu, \mathbf{r}, \hat{\mathbf{n}})}{ds} = & \underbrace{-\mathbf{K}(\nu, \mathbf{r}, \hat{\mathbf{n}})\mathbf{I}(\nu, \mathbf{r}, \hat{\mathbf{n}})}_{\text{Extinction}} + \underbrace{\mathbf{a}(\nu, \mathbf{r}, \hat{\mathbf{n}})B_{\nu,p}(\nu, \mathbf{r})}_{\text{Emission}} \\ & + \underbrace{\int_{4\pi} \mathbf{Z}(\nu, \mathbf{r}, \hat{\mathbf{n}}, \hat{\mathbf{n}}')\mathbf{I}(\nu, \mathbf{r}, \hat{\mathbf{n}}')d\hat{\mathbf{n}}'}_{\text{Scattering}}, \end{aligned} \quad (4.27)$$

where s is the distance along $\hat{\mathbf{n}}$, \mathbf{K} is the extinction matrix, \mathbf{a} is the absorption vector, and \mathbf{Z} is the scattering matrix from Eq. (4.10). The extinction term is a sink term representing both the radiation scattered away and absorbed, completely characterised by \mathbf{K} . The rest of the terms are sources, with the emission term representing thermal radiation by gases and particles, and the scattering term representing radiation scattered into the propagation path. Note that \mathbf{K} , \mathbf{a} , and \mathbf{Z} here are bulk properties, i.e., they are integrated averages over the set of relevant gas

components and particles present in the given volume element. Since the scattering of particles may be dependant on their alignment in space, the parameters must also be averaged with respect to orientation. For details regarding the assumptions of this equation and definitions of the involved quantities the reader is referred to the literature (Mishchenko et al., 2002). Bear in mind that \mathbf{Z} and \mathbf{K} are enough to describe the RTE. The absorption vector is given by the difference of the two matrices according to the relationship

$$\mathbf{K}_{i1} = \int_{4\pi} \mathbf{Z}_{i1} d\hat{\mathbf{n}}' + \mathbf{a}_i, \quad (4.28)$$

which is a generalisation of Eq. 4.12. Nonetheless, all three parameters are often provided explicitly, since on-the-fly calculations of \mathbf{a} can be tedious and prone to numerical discretisation issues related to the integral of the scattering matrix. With the RTE formalised and introduced, the rest of this chapter gives an overview of how the RTE can be solved and what types of input are used.

4.5 Input data

Radiative transfer modelling requires various types of input data to initiate the numerical calculations. The required amount and detail of such data depend on the complexity of the system that is to be modelled and the accuracy of the RT model. This section gives an overview of typical sources used in microwave transfer.

Many RT problems require information on the atmospheric variables such as temperature and humidities. When the purpose is only to get qualitative insight in some phenomena, it is often enough to assume a standardised atmosphere. In Fig. 2.1, the U.S. standard atmosphere was utilised for the temperature profile (Minzner, 1977). Detailed information on the atmospheric state can otherwise be retrieved from global circulation models (GCMs). Operational retrievals must utilise weather forecasting data, while RT modelling of past events can use reanalysis products such as the European Centre for Medium-range Weather Forecasts (ECMWF) reanalysis ERA-5. Reanalysis data comprises historical datasets of land, ocean, and surface that are created by applying a forecasting model to archived observations.

In order to calculate transmission and emission from the atmosphere at various wavelengths, emission lines of atmospheric molecules are also required. A compilation of line-by-line spectroscopic data are provided by the High Resolution Transmission (HITRAN) database (Gordon et al., 2017).

4.5.1 Databases of single scattering properties of ice particles

The main goal of this thesis is the improvement of the representation of hydrometeor microphysics in microwave and sub-millimetre RT. Apart from the database presented in paper A, a number of such databases are currently publicly available. Depending on the target application, they differ in terms of frequencies, shapes, sizes, and format of the provided scattering quantities. The currently most extensive publicly available

databases are: Liu2008 (Liu, 2008), Hong2009 (Hong et al., 2009), Kuo2016 (Kuo et al., 2016), Lu2016 (Lu et al., 2016), Ding2017 (Ding et al., 2017), and Eriksson2018 (paper A, Eriksson et al. (2018)). Table 4.1 gives an overview of these databases. A selection of particle models used in the databases were described in Sec. 3.8. Note that P , provided by the Liu2008 database, is the phase function. It is a simplified version of \mathbf{Z} that only consider the first element of Stokes vector and is consequently only a function of the zenith scattering angle.

The Liu2008 database was the first publicly available SSP database and should be considered a breakthrough in this respect. It includes the sector snowflake model, illustrated in Fig. 3.10. The studies by Geer and Baordo (2014) and Eriksson et al. (2015) argued for the sector snowflake as a good candidate for representing average scattering properties. It is currently used for snow in the ECMWF RT calculations, which have resulted in a clear improvement in the data assimilation of microwave observations of snow and ice clouds. As such, it was included in the Eriksson2018 database as well.

It becomes clear when browsing the databases that while impressive in some aspects, none of the databases available around 2016 fully covers the needs of the Ice Cloud Imager (ICI) instrument. This was a requirement for the Eriksson2018 database. The biggest limitation of the early databases lies in the frequency coverage. The frequency range of MWI, MWS, and ICI goes from 18.7 to 668.2 GHz, which only Ding2017 covers fully. Unfortunately, the aggregate models of the Ding2017 database are too simplistic to work as proxies for snow. Ding2007 also makes use of the single aggregate of the Hong2009 database, shown in Fig. 3.10. As discussed in Sec. 3.8, it does not follow a realistic parameterisation. This argument also applies to the other two Ding2007 aggregates. The Kuo2016 database is more suitable in this respect, employing advanced algorithms for generating pristine and aggregates in a stochastic fashion. Example dendritic snowflakes and aggregates used in Kuo2016 are shown in Fig. 3.11. Unfortunately, neither the phase matrix nor the amplitude scattering matrix is provided in this database, only cross-sections and the asymmetry parameter are available. This limits the Kuo database applicability to simpler RT modelling approaches.

In addition to the frequency coverage, ICI requires SSP data of oriented particles in order to utilise its polarimetric channels. Only the Lu2016 database consider orientations other than totally random orientation (TRO). SSP are calculated by fixing the particle in the horizontal plane and shifting the incidence angles by increments of 10° in zenith and azimuth. However, problems may arise since the incidence angle grid must be considered coarse at large size parameters, i.e., interpolation between grid points will produce large errors and it may be hard to compute average properties accurately. In addition, Lu2016 only considers four frequencies.

Another limitation of several databases is the usage of outdated models for the refractive index. The model by Warren (1984), used by the Hong2009 and Ding2017 databases, has been shown to produce systematic biases in absorption (Eriksson et al., 2015). The model by Ray, 1972, used by the Lu2016 database, is in paper A shown to significantly deviate from more recent models. Overall, the limitations presented here served as the motivation for the database developed and presented in

Table 4.1: Overview of openly available microwave SSP databases. Only the most essential scattering parameters are displayed for each database. For instance, g is omitted if either P , \mathbf{S} , or \mathbf{Z} are provided, because it can be derived from any of those parameters. The included particle types are divided into approximate groups labelled Col (column), Pla (plate), BR (bullet rosette), SL (spheroidal looking, e.g., sphere, spheroid, droxtal, hail, etc.), Agg (aggregate), Sf (snowflake), and Gra (graupel). The refracted indices refer to source publications, i.e., M2006 (Mätzler, 2006), W1984 (Warren, 1984), R1972 (Ray, 1972), and IY2011 (Iwabuchi and Yang, 2011). Note that some of the frequencies, particle types, etc., have been included post-publication.

Database:	Liu2008	Hong2009	Kuo2016	Lu2016	Ding2017	Eriksson2018
Products provided:	P, σ_e	\mathbf{Z}, Q_e	$\sigma_s, \sigma_a, \sigma_b, g$	\mathbf{S}	\mathbf{Z}, Q_e	\mathbf{Z}, σ_e
Orientation:	TRO	TRO	TRO	Fixed	TRO	TRO
Refractive index:	M2006	W1984	Unclear	R1972	IY2011	M2006
Nbr. of frequencies:	22	21	16	4	41	34
Frequency range [GHz]:	[3, 340]	[90, 874]	[3, 190]	[9, 94]	[1, 874]	[1, 886]
Nbr. of temperatures:	5	1	1	1	4	3
Temperature range [°C]:	[-40, 0]	-30	0 (Ambiguous)	0	[-113, -3]	[-83, -3]
Method:	DDA	DDA	DDA	DDA	IF-TM	DDA
Nbr. of particle models:	11	6	29	GMM	IGOM	Mie
Included particles:	2 Sf 2 Pla 3 Col 4 BR	1 Agg 1 Pla 2 Col 1 BR 1 SL	9 Agg 18 Sf 2 Col	5 1 Agg 1 Sf 1 Pla 1 Col 1 Gra	12 3 Agg 1 Pla 2 Col 2 BR 4 SL	33+1 liquid 9 Agg 3 Sf 3 Pla 4 Col 6 BR 5 SL 3 Gr
Nbr. of sizes per particle:	[7, 20]	38	[266, 997]	[30, 660]	24	[30, 45]
D_{veq} range [μm]:	[37, 2,246]	[2, 1,795]	[130, 3,126]	[200, 2,500]	-	[10, 5,293]
D_{max} range [μm]:	[50, 12,454]	[2, 2,000]	[260, 14,260]	[100, 62,580]	[2, 10,000]	[10, 22,860]

paper A and D.

4.6 Solving the radiative transfer equation

The complexity of solving the RT equation varies from case to case. While the generality of the RTE in Eq. 4.28 makes it applicable to most RT problems, it also makes it expensive to solve numerically. For many scenarios, the complexity can be reduced through careful simplification. At microwave frequencies, two scenarios are typically distinguished, the clear-sky and scattering case (in assimilation known as all-sky). This section provides a short overview on how these cases are treated as well as two illustrative examples.

4.6.1 Clear sky

In the clear sky case, scattering in the atmosphere is assumed to be sufficiently small to be neglected. This is not applicable at visible wavelengths, as molecular scattering at those wavelengths is significant (discussed Sec. 4.2). At microwave frequencies, however, molecular scattering can be omitted and the last term in Eq. 4.28 disappears. Cloud droplets at microwave frequencies can often be treated as an absorbing gas as well. Furthermore, it is sometimes sufficient to only consider scalar radiances (omitting polarisation), in which case only the first element of the Stokes vector \mathbf{I} is considered and the RTE is reduced to a scalar equation. Expressed in radiance L_λ , the RTE can then be written as

$$\frac{dL_\lambda}{ds} = -\gamma_a(L_\lambda - B_{\lambda,p}), \quad (4.29)$$

where γ_a is the absorption coefficient in units of m^{-1} . The radiation is attenuated by a rate γ_a and the source term is black-body radiation from the medium along the path of propagation. An analytical solution then exists in the form of

$$L_\lambda(\tau) = \underbrace{L_\lambda(0)e^{-\tau}}_{\text{Boundary}} + \underbrace{\int_0^\tau B_{\lambda,p}(\tau')e^{\tau'-\tau} d\tau'}_{\text{Medium}}. \quad (4.30)$$

The distance coordinate s has been replaced by the *optical depth* τ . A infinite-thin layer of thickness ds has an optical depth of $\gamma_a ds$. The optical depth along the path of propagation is therefore

$$\tau(s) = \int_0^s \gamma_a(s') ds'. \quad (4.31)$$

A layer of thickness s and optical depth $\tau = \tau(s)$ have transmittance

$$t = e^{-\tau}. \quad (4.32)$$

As such, Eq. 4.30 has an intuitive interpretation. The first term, labelled boundary, is the contribution of the radiation entering the boundary at $s = 0$. It is attenuated by a factor $t = e^{-\tau}$ because it has to propagate a distance s through the medium.

The second term instead describes emission in the medium along the propagation path. Each layer $d\tau'$ along the propagation path emits black body radiation equal to $B_{\lambda,p}(\tau')d\tau'$. This contribution must travel through an optical depth $\tau - \tau'$, explaining the transmittance $e^{\tau' - \tau}$ in Eq. 4.30. The problem then consists of deriving γ_a along the propagation path.

At microwave wavelengths it is convenient to rewrite Eq. 4.30 in terms of the brightness temperature T_b . If the Rayleigh-Jeans approximation in Eq. 4.26 applies, Eq. 4.30 becomes

$$T_b(\tau) = T_b(0)e^{-\tau} + \int_0^\tau T(\tau')e^{\tau' - \tau} d\tau'. \quad (4.33)$$

As an illustrative example, Fig. 4.6 shows nadir brightness temperatures T_b as a function of frequency in the microwave and sub-millimetre spectrum at 50 km. Only oxygen and water vapour are considered; the contribution by other gases is small in this band. The temperature profile in Fig. 2.1 is employed to represent the atmosphere in this example. Molecular spectroscopic data are taken from the HITRAN database (Gordon et al., 2017) and the absorption coefficient for each emission line calculated as

$$\gamma_a = Nf(\nu, \nu_0)S_{ij}, \quad (4.34)$$

where S_{ij} is the spectral line intensity, N the molecule number density and f the shape function describing the broadening of the line. Below 60 km only pressure broadening is relevant, which is given by the Lorentzian

$$f(\nu) = \frac{1}{\pi} \frac{\Delta\nu}{\Delta\nu^2 + (\nu - \nu_{0ij})^2}, \quad (4.35)$$

where ν_0 is line centre of the emission line and $\Delta\nu$ the half width at half maximum (HWHM) of f . The HWHM depends on the pressure and temperature, roughly proportional to

$$\Delta\nu \propto T^{-n}p, \quad (4.36)$$

where n is a constant that depends on the emission line and needs to be measured.

Figure 4.7 shows the calculated absorption coefficients for oxygen and water vapour at ground and an altitude of 10 km. The absorption is larger at the ground due to the higher air density. However, at 10 km there is less pressure broadening and some lines reach significant absorption even at this altitude. Oxygen absorption is mostly seen at the higher altitude where water vapour concentration is lower.

Another important feature is the relatively low absorption at the left side of the spectrum. Brightness temperatures below 300 GHz in Fig. 4.6 are to a significant degree composed of surface radiation that is transmitted through the atmosphere (see the difference between total and gas emission). Above 300 GHz virtually all surface radiation is absorbed by the atmosphere. At the strongest emission lines, such as the oxygen line cluster at 60 GHz and vapour line at 557 GHz, the emission comes from the upper part of the atmosphere (about 50 km), where temperature is close to 220 K.

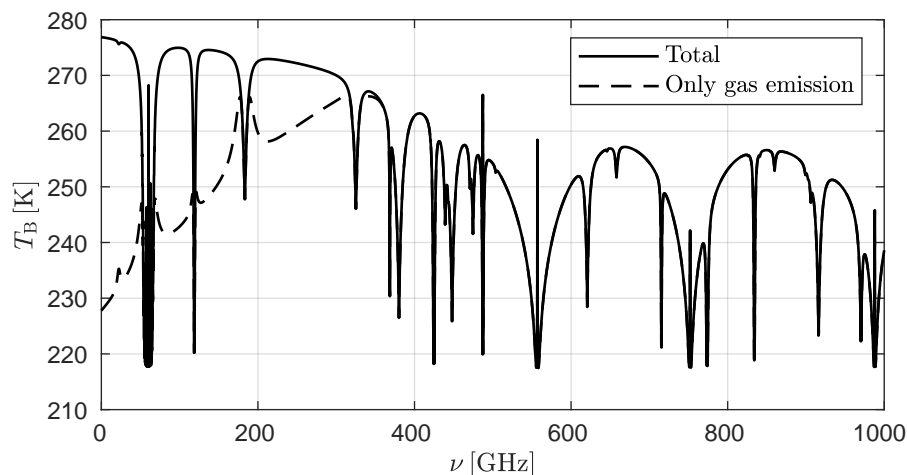


Figure 4.6: Nadir brightness temperatures at microwave frequencies at 50 km. Absorption species included are O_2 and H_2O . The dashed line shows only the contribution from gas emission. The surface temperature is 25°C and the reflectance 0.1.

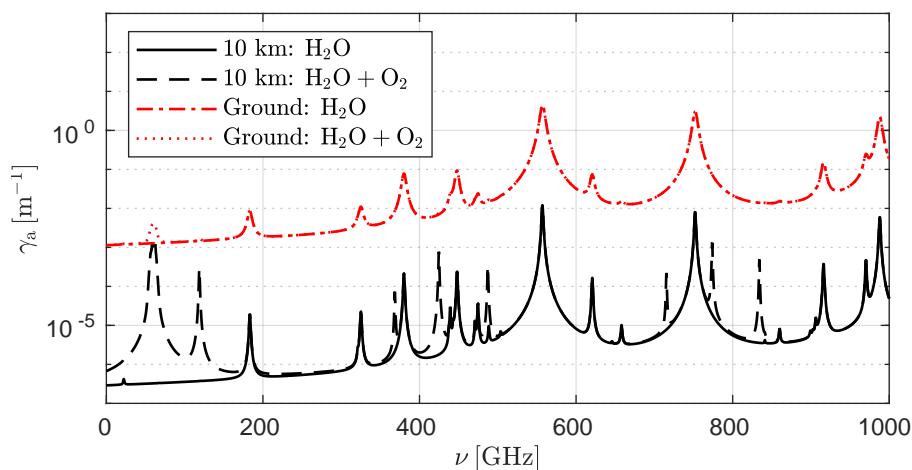


Figure 4.7: Absorption coefficients of O_2 and H_2O at ground and 10 km.

4.6.2 Scattering

Approximate methods exist for cases where scattering needs to be considered. For instance, the two-stream approximation can be used to approximate the transmittance and reflectance of a homogeneous cloud layer. The main idea is to approximate the radiance field by assuming that it only propagates in two discrete directions, typically up- and downwards. For illustrative purposes, a variant of the two-stream approximation⁵ (Petty, 2006) is applied to a thin sub-visual cloud in Fig. 4.8, where absorbance and reflectance as a function of wavelength is shown. The cloud has an ice water content of $2 \times 10^{-4} \text{ g m}^{-3}$, is 1 km thick, and has a temperature of

⁵ The employed variant of the two-stream approximation assumes the radiation field is isotropic, or in other words, diffuse. This assumption is reasonable for outgoing longwave radiation, but is not realistic for solar radiation which can be considered collimated. Nonetheless, the approximation illustrates interesting properties of cirrus clouds.

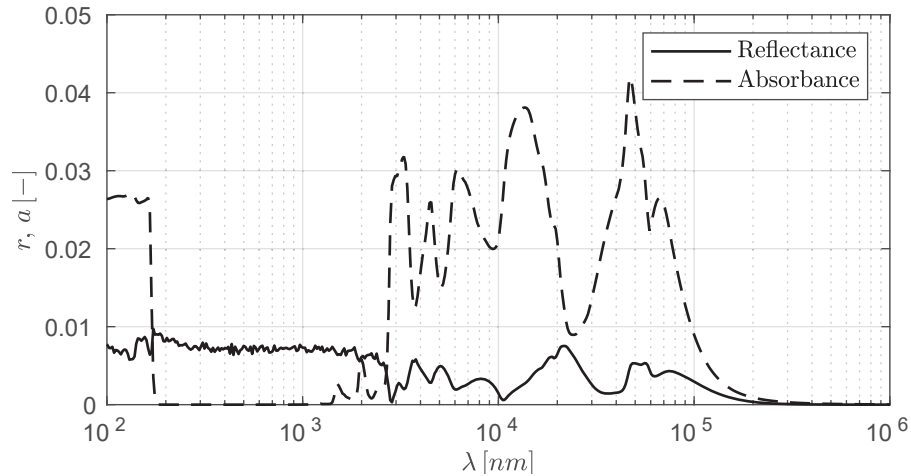


Figure 4.8: Calculated reflectance and absorbance as a function of wavelength for a sub-visual cirrus cloud.

210 K. The parameterisation by McFarquhar and Heymsfield (1997) is used for the particle size distribution and the ice particles are approximated as spheres, with SSP calculated using Mie theory. It is seen that shortwave radiation in the interval 100 to 1000 nm is mostly transmitted; a small portion, less than 1 %, is reflected. The absorption is negligible. For longwave radiation above $3\ \mu\text{m}$ the cloud is relatively absorbing due to the high imaginary refractive index (as indicated by Fig. 4.2). In summary, sub-visual cirrus are relatively transparent to incident solar radiation, but absorb significant amount of outgoing longwave radiation. In turn, cirrus clouds emit radiation out to space, but at a much colder temperature compared to the surface, explaining why such clouds have a positive radiative forcing.

In cases where multiple scattering must be modelled with higher accuracy, there are a number of different methods. The issue of multiple scattering is related to the integrand of the scattering term in the RTE (Eq. 4.28), which sums up the radiation scattered into the path of propagation. The discrete ordinate method can be used for a plane parallel media, i.e., a media composed of horizontal homogeneous layers. The scattering integral is approximated by a quadrature formula of order N that corresponds to the number of streams, i.e., discrete directions along which the radiations can propagate. For $N = 2$, the discrete ordinate method is reduced to the two-stream approximation. When the media is not plane-parallel (or not a sufficiently good approximation), the Monte-Carlo (MC) method can be used instead. In short, the MC method simulates trajectories of individual light packages probabilistically. Acceptable accuracy may require a large amount of simulated trajectories, and the MC method is therefore computationally expensive.

Chapter 5

Microwave and sub-millimetre remote sensing

It is now time to briefly discuss the microwave (MW) and sub-millimetre (sub-MM) sensors relevant for observations of hydrometeors. The main advantage of MW instruments is that they can penetrate clouds and precipitation and measure their densities (i.e., liquid or ice water content). Optical instruments, can only see the borders of the clouds. However, a MW instrument is limited by its angular resolution $\Delta\theta$, determined by the size D_a of its antenna according to (Rees, 2001)

$$\Delta\theta \approx 1.22 \frac{\lambda}{D_a}. \quad (5.1)$$

In other words, bigger antennas and smaller wavelengths result in better resolution. Two categories of MW sensors are used. Passive sensors measure the radiation emitted from the surface and atmosphere. Active sensors both transmit radiation and detect the back-scattered radiation.

5.1 Platforms

The advantages and disadvantages of platforms for remote sensing are mostly similar to those of in-situ (Sec. 3.1). Ground-based remote sensing instruments are relatively cheap, easy to build, and maintain, but are limited in their locality. Ground-based weather radars supply weather forecasting with observations of precipitation and are used to monitor hazardous weather. Aircraft-based remote sensing offers flexibility but is instead expensive to operate; it is more suited for scientific or validation studies. In contrast to in-situ instrumentation, remote sensing can also be performed from satellites. Satellites can be very expensive, in the order of hundred of millions of euros. Great care has to go into the design, testing, and validation of instruments mounted on the satellite. Once in space, the amount of adjustments and maintenance is limited. However, satellite remote sensing compensate for the costs by the amount of data it provides. This input is invaluable to weather and climate applications and can not be provided through alternative means.

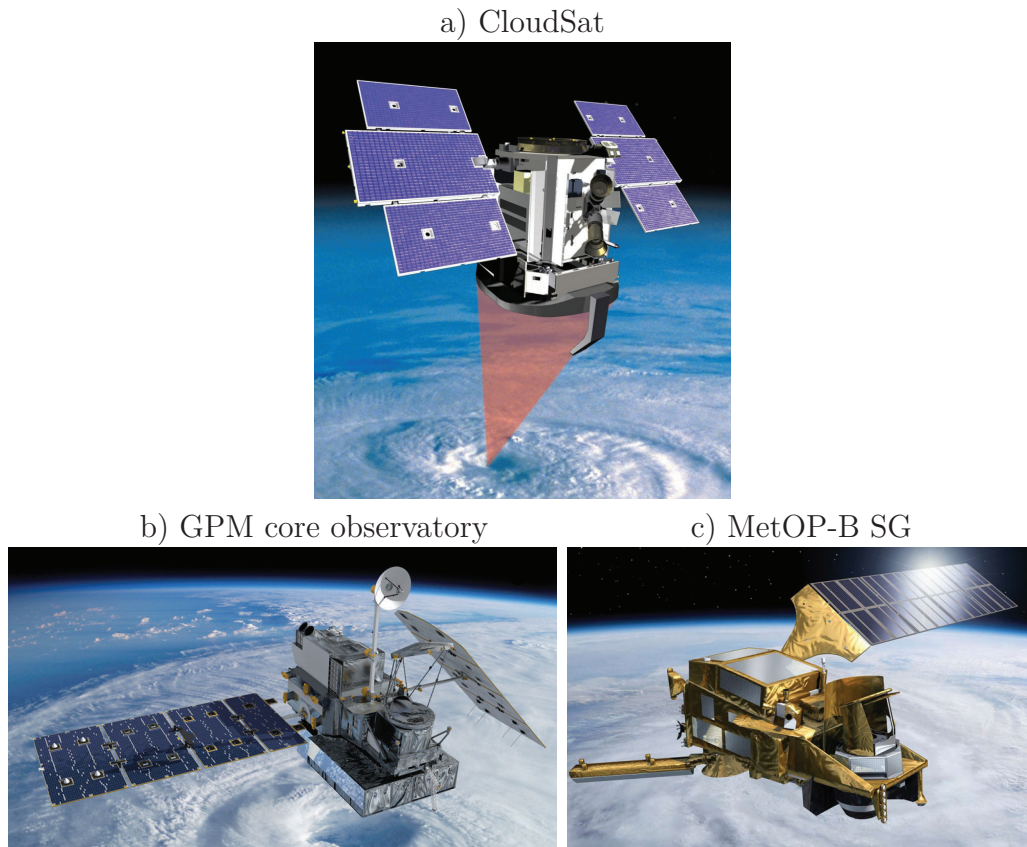


Figure 5.1: The satellites used in this thesis. Images by NASA and EUMETSAT.

Satellites are distinguished by their orbit altitude. The altitude of geostationary orbits are approximately 36×10^3 km. At this altitude the orbit is synced with the rotation of Earth and the satellite is permanently positioned over a specific point above the equator. Geostationary satellites are useful for now-casting (weather forecasting on the very shortscale, up to 2 hours) and monitoring of hazardous weather or forest fires, for instance. However, they are not useful for MW remote sensing, due to the limitation in ground resolution. The footprint diameter is approximately

$$\Delta d = R\Delta\theta = \frac{R\lambda}{D_a}, \quad (5.2)$$

where R is the range to the target. In order to achieve a footprint of 44 km at 60 GHz the antenna diameter would have to be 4 m, which is very large for spaceborne antennas. Geostationary satellites are therefore more suited for visible (VIS) and infrared (IR) imaging.

Microwave instruments are instead mounted on lower Earth orbit (LEO) satellites. A particularly useful choice for Earth-observing satellites is the sun-synchronous orbits. They are nearly polar orbits (inclination close to 90°), which maintain a fixed relative angle relative to the Sun, meaning the satellite always passes over a certain latitude at a specific solar time. Figure 5.1 shows the main satellites considered in this thesis; they are all polar orbiting satellites.

5.2 Active remote sensing

Active sensors have multiple advantages over passive sensors. From the return time of the transmitted signal, the distance to the target can be inferred. Active sensors therefore have high range resolution. The power of the received radiation contains information on the target's back-scattering cross-section. They operate in different bands. Lidars (light detection and ranging) operate at ultraviolet, VIS, or IR wavelengths and illuminate the target with a laser. The CALIOP (Cloud-Aerosol Lidar with Orthogonal Polarisation) aboard the CALIPSO (Cloud-Aerosol Lidar and Infrared Pathfinder Satellite Observations) satellite (Stephens et al., 2018) operates at VIS to near-IR wavelengths and is mainly suitable for measuring ice particles smaller than 100 μm (Buehler et al., 2007). The signal attenuates quickly in optically thick clouds and has limited penetration capabilities beyond that of cirrus clouds.

Radars instead transmit at the longer MW wavelengths and are less sensitive to small hydrometeors. They have better penetration capabilities than lidars and are useful for profiling thick clouds and precipitation. The CloudSat satellite carries the Cloud Profiling Radar (CPR) that operates at 94.1 GHz, mostly sensitive to larger hydrometeors. As a part of the satellite constellation *A-train*, CloudSat and CALIPSO have been used to conduct co-located measurements of ice clouds. The DARDAR (raDAR/liDAR) ice cloud product is a result of those measurements (Cazenave et al., 2019). CloudSat data and the DARDAR product were utilised in paper C to generate detailed two-dimensional scenes of ice water content (IWC). Another limitation of the CloudSat radar is the small horizontal coverage due to its fixed line-of-sight angle (the CloudSat CPR antenna diameter is 1.85 m) and narrow beam width. Ground-based weather radars do not face this problem, but are instead limited in their locality. Another example of satellite-borne radars is the dual-frequency precipitation radar (DPR) carried by the GPM (Global Precipitation Measurement) core observatory (Hou et al., 2014). It operates at longer wavelengths than CloudSat (13.6 and 35.5 GHz) and is less sensitive to ice hydrometeors than CloudSat (Casella et al., 2017). Presently, there is no other radar in space relevant for measuring ice hydrometeors.

In radar meteorology the returned signal is usually given in terms of the effective radar reflectivity Z_e (has units mm^6m^{-3}). It is given as

$$Z_e = \frac{\lambda^4}{\pi^5 |K_w|^2} \int_0^\infty \sigma_b n(D) dD, \quad (5.3)$$

where $K_w = (n_w^2 - 1) / (n_w^2 + 2)$ is the dielectric factor and n_w is the refractive index of water at wavelength λ . The back-scattering coefficient σ_b is given by Eq. 4.16. Z_e is normalised in such a way that the return of 1 mm rain drop in an unit volume gives $Z_e = 1 \text{ mm}^6\text{m}^{-3}$. It is typically given in decibels, in which case it is labelled dBZ. Equation 5.3 is relatively simple to invert for the purpose of retrievals. However, multiple scattering and attenuation will complicate the retrievals at higher frequencies.

5.3 Passive remote sensing

Microwave sensors are typically designed with scanning capabilities, either conically or across-track scanning, giving them large horizontal coverage. However, they suffer from poor vertical resolution, since measured signals depend on a large part of the atmospheric column. Retrieval of physical quantities from passive radars is therefore more complicated compared to radars. As implied by the solution of radiative transfer (RT) equation in clear-sky conditions (Eq. 4.30), the signal is the weighted mean of the contribution by the atmosphere and the surface to the observed brightness temperature. Where the radiation originates from depends on the optical depth of the medium, as shown in Fig. 4.6. Vertical information can therefore be retrieved through careful selection of frequency channels, e.g., around the edges of an emission line. This is the principle behind atmospheric sounding (Rees, 2001). For instance, the oxygen lines at 60 GHz are useful for temperature sounding. Similar principles hold for the retrieval of the density of clouds or precipitation. Liquid droplets are very small and are mostly absorbing at MWs, while for ice hydrometeors the situation is more complicated due to scattering. Particle size distribution (PSD), shape, and orientation can generally not be retrieved directly by remote sensing and assumptions on these must be made. It is therefore important that hydrometeors are represented in a realistic and accurate manner in order to optimise the utilisation of MW remote sensing.

The GPM core satellite (Hou et al., 2014) carries apart from the DPR the GPM microwave imager (GMI), facilitating combined passive and active retrievals of precipitation (Ringerud et al., 2019). It has channels from 6 to 183 GHz and its data were employed in Paper C in order to test and validate the scattering database in paper A. Other operational sensors with channels up to 183 GHz that have been used for IWC retrievals, include the Special Sensor Microwave Imager/Sounder (SSMIS) (Sun and Weng, 2012) and the Advanced Microwave Sounding Unit (AMSU) (Surussavadee and Staelin, 2009). The 183 GHz channels are mostly sensitive to larger ice particles, approximately 1 mm (Buehler et al., 2007). Sensitivity to smaller ice particles found in ice clouds, can be achieved through sub-MM frequencies. This has been demonstrated by the limb sounding instruments of Aura Microwave Limb Sounder (MLS) (Wu et al., 2006), superconducting Sub-millimetre Limb Emission Sounder (SMILES), and Odin sub-millimetre radiometer (SMR) (Eriksson et al., 2014).

Currently, no operational satellite sensors above 190 GHz exist. This situation is about to change. In 2023 the MetOp-B SG (Meteorological Operational Satellite - Second Generation) satellite is scheduled for launch (Eriksson et al., 2020). It will carry the Ice Cloud Imager (ICI), a conically scanning radiometer with 11 channels from 183 to 664 GHz. Two channels, at 243 and 664 GHz, will measure both h- and v-polarisation and will be useful for the detection of oriented hydrometeors. ICI will also therefore provide unprecedented global observations of ice hydrometeors. It will complement CloudSat with accurate estimates of ice water path and its large horizontal coverage (Pfreundschuh et al., 2019). In addition, MetOp-B SG will carry the MicroWave Imager (MWI), which is a conically scanning radiometer. MWI

channels range up to 183 GHz. Together, MWI and ICI can provide collocated measurements and be validated against each other. They will provide valuable input to weather forecasts around the world through data assimilation.

Chapter 6

Summary and outlook

6.1 Paper A

The bulk of the work presented in this paper was produced as a part of an EUMETSAT study, intended to support the upcoming ICI, MWI, and MWS (MicroWave Sounder) aboard the second generation of MetOp satellites. Utilisation of these sensors requires accurate single scattering properties (SSP) data, severely lacking at the time. A database was thus developed with the following requirements in mind: i) Inclusion of realistic, complex shaped particles, especially that of large aggregates; ii) A broad frequency spectrum, covering the channels of ICI, MWI, and MWS; and iii) A format general enough so that polarimetric measurements can be utilised.

Single scattering properties data, covering 34 different particle models, 34 frequencies from 1 to 886.4 GHz, and 3 temperatures, were produced using the discrete dipole approximation (DDA) and stored in a database. Available particle sizes range from 10 μm to 2 cm, depending on the particle model. In this respect, the database is the most extensive released to this date. Covered particle models range from pristine crystals such as hexagonal plates, columns, and bullet rosettes, to complex aggregates, graupel, and hail. Most of the aggregates were generated using an aggregation simulation software that was developed internally (by our group), using different constituent crystal axis ratios and sizes. Clear differences in scattering properties could be seen between these aggregates. The database is publicly available by Zenodo, an open-access data repository operated by Cern, and is provided with data interfaces in MATLAB and Python, in order to increase the ease of use. So far, only totally random orientation (TRO) is covered, but the azimuthally randomly oriented (ARO) SSP data presented in Paper D will be included as well.

6.2 Paper B

The database in paper A includes aggregates generated in a realistic and sophisticated manner, for which clear differences could be discerned in terms of scattering properties. The motivation for this study is to investigate, in a more systematic manner, what aggregate aspects are important in terms of scattering properties. Using the

aggregation software developed for the database, 11 simulations of aggregates with varying constituent crystal axial ratios were performed, resulting in a large set of aggregate data of varying characteristics. Consequently, the aggregates' morphologies and their link to the associated scattering properties was investigated. In contrast to the database in paper A, all scattering properties are calculated assuming horizontally aligned particles.

Radar cross-sections (at 13.4, 35.6, and 94.1 GHz) and extinction cross-sections (at 183.3, 325.2, and 664 GHz) were found to be strongly influenced by the crystal axis ratio, effective density, aerodynamic area, and the number of constituent crystals in the aggregates. This was not found for the aggregate aspect ratio. Bulk properties calculated at radar and sub-millimetre frequencies were also significantly influenced by the aggregate shape parameters. For instance, the radar triple frequency signatures saw a clear dependence on the effective density, consistent with reports from literature. Extinction at 664 GHz is relatively insensitive to shape, indicating its suitability for retrieving ice mass in comparison to 183 GHz. It was also found that the bulk properties are less sensitive to aggregate shape, if they are expressed in snowfall rate instead of ice water content. In other words, snowfall rate could potentially be retrieved at a higher accuracy than ice water content.

6.3 Paper C

Paper C proposes and demonstrates a method to analyse and validate the SSP data developed in paper A. The intent is to determine which particle models give the best agreement in radiative transfer (RT) simulations in comparison to real satellite observations. The main feature of this study is that both passive and active observations are considered simultaneously. A limited geographic area in the tropical Pacific Ocean was considered.

The modelling system is composed of three main steps. Firstly, ice water content is retrieved from 94.1 GHz radar observations by the CloudSat satellite which are then converted to synthetic two-dimensional scenes. Complementary atmospheric data are taken from the ERA-Interim reanalysis product. In the second step, these scenes are used as input in passive RT simulations, assuming different combinations of selected particle types from the database and particle size distributions (PSD) from different external sources. The simulations mimic real satellite observations by the GPM (Global Precipitation Measurement) Microwave Imager (GMI) at 166, 186.31, and 190.31 GHz. Finally, distributions of simulated and real observations of brightness temperature are compared statistically.

It is found that the radar retrievals and passive forward simulations are sensitive to assumed particle type and PSD when considered separately. On the other hand, when the full modelling system is used, simulated and real passive observations agree well, for most combinations of PSD and particle model. This indicates the robustness of the radar retrievals and the passive simulations. However, the reduced uncertainty to particle model and PSD makes it difficult to find a microphysical model that performs better than any of other models. It could be argued that the 94.1 GHz radar and the passive GMI channels are too similar to each other, i.e., they do not

provide complementary information on microphysics. One particle model, a column aggregate, gives marginally better results than the other models for cases of deep convection. In contrast, the tested air-ice mixture spheroid model performs relatively poorly.

The modelling system was also applied to selected channels of the upcoming Ice Cloud Imager (328.65, 334.65, 668.2 GHz). It is not possible to compare these simulations to real observations yet. However, the simulations at ICI frequencies are promising, because they reveal much larger discrepancies in response to assumed particle model. In other words, the 94.1 GHz radar and 668.2 GHz likely contain complementary information on microphysics. The study therefore points to the potential of combining CloudSat-like radars and ICI observations to constrain microphysics, using the method demonstrated in this paper.

6.4 Paper D

Despite the fact that dual-polarisation microwave observations show clear evidences of oriented particles, the amount of publicly available SSP data for such particles are limited. This paper is an attempt at remedying the situation, by providing ARO scattering properties of a plate crystal and aggregate particle model. The DDA method was used to calculate the SSP, while a self-developed orientation averaging method was employed to derive the ARO SSP. The data serve as an extension to the database presented in paper A. As such, the frequency and temperature grids of the SSP are the same as in that database.

For testing and validation purposes, the SSP data were applied in passive forward simulations at the dual polarisation channel of GMI (166 GHz). The large plate aggregate particle model was applied to snow and the plate crystal model to cloud ice. The simulated observations were then compared to the real satellite observations of oriented ice particles. Previous studies show characteristic polarisation differences of up to 10 K for scenes with clouds (Defer et al., 2014; Gong and Wu, 2017). It is found that the oriented SSP data can indeed reproduce these polarisation signals. With this dataset, retrievals using the upcoming ICI can hopefully give us additional insights on clouds and ice hydrometeors.

6.5 Paper E

In this paper, the attention is turned towards liquid hydrometeors. While liquid cloud droplets are small and spherical, the shape of a rain drop is distorted due to aerodynamic drag as it increases in mass and gain in fall-speed. This effect is often not accounted for in microwave RT and no publicly available SSP data for non-spheroidal liquid drops exist.

In this study, the SSP of non-spheroidal rain drops were calculated using the T-matrix method and compiled into an openly available database. The drop shapes were calculated numerically using the model from Chuang and Beard (1990), which represents the drops using Chebyshev polynomials. The SSP of these Chebyshev

drops were compared to mass-equivalent spherical and spheroidal (equal aspect ratio) drops. The impact of drop shape upon SSP is not as large as is usually the case for ice hydrometeors. However, for heavy rainfall there is a noticeable effect. For instance, significant differences between the Chebyshev and reference drops are found for the zenith radar reflectivity (see Eq. 5.3) at 94.1 GHz and side-looking differential radar reflectivity at 5 GHz. In those cases the differences are almost 1 dBZ at rainfalls around 10 mm h^{-1} . Furthermore, simulations of passive microwave brightness temperatures showed differences of up to 1.3 K for frequencies below 150 GHz. The overall recommendation is to use a non-spheroidal drop-model for radar measurements of heavy rain-fall and passive measurements below 150 GHz.

6.6 Conclusions and outlook

The overarching goal of this thesis is to improve the representation of hydrometeors in microwave and sub-millimetre RT. An extensive SSP database for totally randomly oriented ice hydrometeors was created in the first half of the PhD project (paper A). It was later complemented with SSP of oriented particles (paper D) and liquid drops (paper E). The database will be employed, at least, as input to the radiative transfer model RTTOV-SCATT (Radiative Transfer for TOVS¹ - SCATTering), which is used by ECMWF for data assimilation of microwave radiances. It will also be used for future ICI, MWI, and MWS retrieval products.

There is room for improvements in the database, both in terms of data quality and covered features. In the future the following work is suggested to improve the database:

- There are indications on that the database SSP are not accurate enough for radar applications. The back-scattering cross-section is in comparison to the extinction cross-section more sensitive to the convergence criterion used in the DDA method. It is therefore recommended that the SSP are re-calculated for frequencies below 100 GHz using stricter convergence criteria.
- While originally planned, ice particles that are partially melted have still not been included in the database due to time restrictions and other priorities. Scattering is strongly affected by melting, due to the strong difference in dielectric properties of ice and liquid water, giving rise to the high radar reflectivities observed inside the melting layer, commonly referred to as the radar “bright band” (Wallace and Hobbs, 2006). As previous studies have shown, SSP of melting ice particles are challenging to calculate due to the higher refractive index of liquid water, resulting in relatively long computation times (Ori et al., 2014; Johnson et al., 2016).

Future activities should also be aimed at further exploring the performance of the developed SSP data. In specific, the issue that needs to be addressed is which

¹ TOVS (TIROS Operational Vertical Sounder), an atmospheric sounding system aboard the TIROS-N (Television infrared observation satellite - next generation) series of satellites.

particle models work best for different conditions. The study in paper C found that most of the considered particles could model GMI and CloudSat observations of tropical Pacific clouds. Sub-millimetre observations, as will be provided by ICI, will be crucial in further constraining the particle models. The SSP database has been employed in other modelling studies that considered sub-MMs. Fox et al., 2019 employed airborne lidar, in-situ instrumentation and, the International Sub-millimetre Airborne Radiometer (ISMAR) in order to validate RT simulations using SSP from the database. It was found that the database particles can reproduce the radiometer observations up to 664 GHz. The particle model that performed best was highly dependant on which part of the cloud that was observed. Notably, the sector snowflake (see Fig. 3.10), which is currently used in the ECMWF data assimilation system, was found to be significantly inconsistent with observations between 325 and 664 GHz. Pfreundschuh et al. (2019) studied the potential benefit of co-located ICI and CloudSat-like radar observations, considering one case of a mesoscale convective system in the tropics and one case of low-level cloud in the North Atlantic. The scenes were produced using the Global Environmental Multiscale (GEM) model. They preferred the large plate aggregate as an intermediate model.

In short, more studies are required in order to constrain the particle models. It would be beneficial with more ISMAR-like observations that combine in-situ and remote sensing observation of clouds. The aforementioned satellite-based studies could also be extended to consider other frequencies than MW and sub-MM. Options include passive infrared or lidar measurements, which are mainly useful to detect small ice crystals. This will require the inclusion of infrared frequencies in the database.

6.7 Contribution to papers

Papers A, C, D, and E contain comments on author contribution. For paper B, I (Robin Ekelund) have simulated the aggregate particles, calculated the SSP, performed the analysis, and written the article's text.

Bibliography

- Auer Jr., August H. and Donald L. Veal (1970). “The Dimension of Ice Crystals in Natural Clouds”. In: *J. Atmos. Sci.* 27.6, pp. 919–926.
- Bailey, Matthew P and John Hallett (2009). “A Comprehensive Habit Diagram for Atmospheric Ice Crystals: Confirmation from the Laboratory, AIRS II, and Other Field Studies”. In: *J. Atmos. Sci.* 66.9, pp. 2888–2899.
- Baran, Anthony J. (2009). “A review of the light scattering properties of cirrus”. In: *J. Quant. Spectrosc. Radiat. Transfer* 110.14-16, pp. 1239–1260.
- Baum, Bryan A., Ping Yang, Andrew J. Heymsfield, Carl G. Schmitt, Yu Xie, Aaron Bansemer, Yong-Xiang Hu, and Zhibo Zhang (2011). “Improvements in Shortwave Bulk Scattering and Absorption Models for the Remote Sensing of Ice Clouds”. In: *J. Appl. Meteorol. Clim.* 50.5, pp. 1037–1056.
- Bohren, Craig F. and Louis J. Battan (1980). “Radar Backscattering by Inhomogeneous Precipitation Particles”. In: *J. Atmos. Sci.* 37.8, pp. 1821–1827.
- Bony, Sandrine et al. (2015). “Clouds, circulation and climate sensitivity”. In: *Nat. Geosci.* 8.4, pp. 261–268.
- Borys, Randolph D., Douglas H. Lowenthal, Stephen A. Cohn, and William O. J. Brown (2003). “Mountaintop and radar measurements of anthropogenic aerosol effects on snow growth and snowfall rate”. In: *Geophys. Res. Lett.* 30.10.
- Brown, Philip R. A. and Peter N. Francis (1995). “Improved Measurements of the Ice Water Content in Cirrus Using a Total-Water Probe”. In: *J. Atmos. Oceanic Technol.* 12.2, pp. 410–414.
- Buehler, S A et al. (2012). “Observing ice clouds in the submillimeter spectral range: the CloudIce mission proposal for ESA’s Earth Explorer 8”. In: *Atmos. Meas. Tech.* 5.7, pp. 1529–1549.
- Buehler, S. A. et al. (2007). “A concept for a satellite mission to measure cloud ice water path, ice particle size, and cloud altitude”. In: *Q. J. R. Meteorol. Soc.* 133.S2, pp. 109–128.
- Casella, Daniele, Giulia Panegrossi, Paolo Sanò, Anna Cinzia Marra, Stefano Dietrich, Benjamin T. Johnson, and Mark S. Kulie (2017). “Evaluation of the GPM-DPR snowfall detection capability: Comparison with CloudSat-CPR”. In: *Atmos. Res.* 197, pp. 64–75.
- Cazenave, Quitterie, Marie Ceccaldi, Julien Delanoë, Jacques Pelon, Silke Groß, and Andrew Heymsfield (2019). “Evolution of DARDAR-CLOUD ice cloud retrievals: new parameters and impacts on the retrieved microphysical properties”. In: *Atmos. Meas. Tech.* 12.5, pp. 2819–2835.

- Chuang, Catherine C. and Kenneth V. Beard (1990). “A Numerical Model for the Equilibrium Shape of Electrified Raindrops”. In: *J. Atmos. Sci.* 47.11, pp. 1374–1389.
- Coddington, Odele, Judith L. Lean, Doug Lindholm, Peter Pilewski, Martin Snow, and NOAA CDR Program (2015). *NOAA Climate Data Record (CDR) of Solar Spectral Irradiance (SSI), NRLSSI Version 2*. doi:10.7289/V51J97P6 [8 Jan 2020].
- Connolly, P. J., C. P. R. Saunders, M. W. Gallagher, K. N. Bower, M. J. Flynn, T. W. Chouarton, J. Whiteway, and R. P. Lawson (2005). “Aircraft observations of the influence of electric fields on the aggregation of ice crystals”. In: *Q. J. R. Meteorol. Soc.* 131.608, pp. 1695–1712.
- Defer, Eric, Victoria S. Galligani, Catherine Prigent, and Carlos Jimenez (2014). “First observations of polarized scattering over ice clouds at close-to-millimeter wavelengths (157 GHz) with MADRAS on board the Megha-Tropiques mission”. In: *J. Geophys. Res. Atmos.* 119.21, pp. 12, 301–12, 316.
- Ding, Jiachen, Lei Bi, Ping Yang, George W Kattawar, Fuzhong Weng, Quanhua Liu, and Thomas Greenwald (2017). “Single-scattering properties of ice particles in the microwave regime: Temperature effect on the ice refractive index with implications in remote sensing”. In: *J. Quant. Spectrosc. Radiat. Transfer* 190, pp. 26–37.
- Draine, Bruce T. and Piotr J. Flatau (1994). “Discrete-Dipole Approximation For Scattering Calculations”. In: *J. Optical Soc. o. Am. A* 11.4, p. 1491.
- Duncan, David Ian and Patrick Eriksson (2018). “An update on global atmospheric ice estimates from satellite observations and reanalyses”. In: *Atmos. Chem. Phys.* 18.15, pp. 11205–11219.
- Ellison, W. J. (2007). “Permittivity of pure water, at standard atmospheric pressure, over the frequency range 0–25 THz and the temperature range 0–100°C”. In: *J. Phys. Chem. Ref. Data.* 36.1, pp. 1–18.
- Eriksson, P., R. Ekelund, J. Mendrok, M. Brath, O. Lemke, and S. A. Buehler (2018). “A general database of hydrometeor single scattering properties at microwave and sub-millimetre wavelengths”. In: *Earth Syst. Sci. Data* 10.3, pp. 1301–1326.
- Eriksson, P., M. Jamali, J. Mendrok, and S. A. Buehler (2015). “On the microwave optical properties of randomly oriented ice hydrometeors”. In: *Atmos. Meas. Tech.* 8.5, pp. 1913–1933.
- Eriksson, P., B. Rydberg, H. Sagawa, M. S. Johnston, and Y. Kasai (2014). “Overview and sample applications of SMILES and Odin-SMR retrievals of upper tropospheric humidity and cloud ice mass”. In: *Atmos. Chem. Phys.* 14.23, pp. 12613–12629.
- Eriksson, Patrick, Bengt Rydberg, Vinia Mattioli, Anke Thoss, Christophe Accadia, Ulf Klein, and Stefan A. Buehler (2020). “Towards an operational Ice Cloud Imager (ICI) retrieval product”. In: *Atmos. Meas. Tech.* 13.1, pp. 53–71.
- Field, P. R., A. J. Heymsfield, and A. Bansemer (2006). “Shattering and Particle Interarrival Times Measured by Optical Array Probes in Ice Clouds”. In: *J. Atmos. Oceanic Technol.* 23.10, pp. 1357–1371.

- Field, Paul R, Andrew J Heymsfield, and Aaron Bansemer (2007). “Snow size distribution parameterization for midlatitude and tropical ice clouds”. In: *J. Atmos. Sci.* 64.12, pp. 4346–4365.
- Fox, Stuart, Jana Mendrok, Patrick Eriksson, Robin Ekelund, Sebastian J O’shea, Keith N Bower, Anthony J Baran, R Chawn Harlow, and Juliet C Pickering (2019). “Airborne validation of radiative transfer modelling of ice clouds at millimetre and sub-millimetre wavelengths”. In: *Atmos. Meas. Tech.* 12, pp. 1599–1617.
- Garnett, J. C. M. (1904). “Colours in metal glasses and in metallic films”. In: *Phil. Trans. R. Soc. Lond. A* 203.359-371, pp. 385–420.
- Garrett, T J, C Fallgatter, K Shkurko, and D Howlett (2012). “Fall speed measurement and high-resolution multi-angle photography of hydrometeors in free fall”. In: *Atmos. Meas. Tech.* 5.11, pp. 2625–2633.
- Garrett, Timothy J., Sandra E. Yuter, Cale Fallgatter, Konstantin Shkurko, Spencer R. Rhodes, and Jason L. Endries (2015). “Orientations and aspect ratios of falling snow”. In: *Geophys. Res. Lett.* 42.11, pp. 4617–4622.
- Geer, A. J. and F. Baordo (2014). “Improved scattering radiative transfer for frozen hydrometeors at microwave frequencies”. In: *Atmos. Meas. Tech.* 7.6, pp. 1839–1860.
- Geer, A. J., F. Baordo, N. Bormann, P. Chambon, S. J. English, M. Kazumori, H. Lawrence, P. Lean, K. Lonitza, and C. Lupu (2017). “The growing impact of satellite observations sensitive to humidity, cloud and precipitation”. In: *Q. J. R. Meteorol. Soc.* 143.709, pp. 3189–3206.
- Gong, Jie and Dong L Wu (2017). “Microphysical properties of frozen particles inferred from Global Precipitation Measurement (GPM) Microwave Imager (GMI) polarimetric measurements”. In: *Atmos. Chem. Phys.* 17.4, pp. 2741–2757.
- Gordon, I.E. et al. (2017). “The HITRAN2016 molecular spectroscopic database”. In: *J. Quant. Spectrosc. Radiat. Transfer* 203, pp. 3–69.
- Gravner, Janko and David Griffeath (2009). “Modeling snow-crystal growth: A three-dimensional mesoscopic approach”. In: *Phys. Rev. E* 79.1, p. 011601.
- Helten, M., H. G. J. Smit, D. Kley, J. Ovarlez, H. Schlager, R. Baumann, U. Schumann, P. Nedelec, and A. Marengo (1999). “In-flight comparison of MOZAIC and POLINAT water vapor measurements”. In: *J. Geophys. Res. Atmos.* 104.D21, pp. 26087–26096.
- Heymsfield, Andrew J., Sharon Lewis, Aaron Bansemer, Jean Iaquina, Larry M. Miloshevich, Masahiro Kajikawa, Cynthia Twohy, and Michael R. Poellot (2002). “A General Approach for Deriving the Properties of Cirrus and Stratiform Ice Cloud Particles”. In: *J. Atmos. Sci.* 59.1, pp. 3–29.
- Heymsfield, Andrew J. and Larry M. Miloshevich (2003). “Parameterizations for the Cross-Sectional Area and Extinction of Cirrus and Stratiform Ice Cloud Particles”. In: *J. Atmos. Sci.* 60.7, pp. 936–956.
- Heymsfield, Andrew J. et al. (2017). “Cirrus Clouds”. In: *Meteorol. Monogr.* 58, pp. 2.1–2.26.
- Hong, G., P. Yang, B. A. Baum, A. J. Heymsfield, F. Weng, Q. Liu, G. Heygster, and S. A. Buehler (2009). “Scattering database in the millimeter and submillimeter

- wave range of 100-1000 GHz for nonspherical ice particles”. In: *J. Geophys. Res.* 114, D06201, p. 6201.
- Hou, Arthur Y, Ramesh K Kakar, Steven Neeck, Ardeshir A Azarbarzin, Christian D Kummerow, Masahiro Kojima, Riko Oki, Kenji Nakamura, and Toshio Iguchi (2014). “The global precipitation measurement mission”. In: *Bull. Amer. Met. Soc.* 95.5.
- IPCC (2007). *Climate Change 2007: The Physical Science Basis. Contribution of Working Group I to the Fourth Assessment Report of the Intergovernmental Panel on Climate Change*. Ed. by S. Solomon, D. Qin, M. Manning, Z. Chen, M. Marquis, K.B. Averyt, M. Tignor, and H.L. Miller. Cambridge, United Kingdom and New York, NY, USA: Cambridge University Press.
- IPCC (2013a). “Clouds and Aerosols”. In: *Climate Change 2013: The Physical Science Basis. Contribution of Working Group I to the Fifth Assessment Report of the Intergovernmental Panel on Climate Change*. Ed. by T.F. Stocker, D. Qin, G.-K. Plattner, M. Tignor, S.K. Allen, J. Boschung, A. Nauels, Y. Xia, V. Bex, and P.M. Midgley. Cambridge, United Kingdom and New York, NY, USA: Cambridge University Press. Chap. 7, pp. 571–658.
- IPCC (2013b). *Introduction*. Ed. by T.F. Stocker, D. Qin, G.-K. Plattner, M. Tignor, S.K. Allen, J. Boschung, A. Nauels, Y. Xia, V. Bex, and P.M. Midgley. Cambridge, United Kingdom and New York, NY, USA: Cambridge University Press. Chap. 1, pp. 119–158.
- IPCC (2013c). “Summary for Policymakers”. In: *Climate Change 2013: The Physical Science Basis. Contribution of Working Group I to the Fifth Assessment Report of the Intergovernmental Panel on Climate Change*. Ed. by T.F. Stocker, D. Qin, G.-K. Plattner, M. Tignor, S.K. Allen, J. Boschung, A. Nauels, Y. Xia, V. Bex, and P.M. Midgley. Cambridge, United Kingdom and New York, NY, USA: Cambridge University Press. Chap. SPM, pp. 1–30.
- Iwabuchi, Hironobu and Ping Yang (2011). “Temperature dependence of ice optical constants: Implications for simulating the single-scattering properties of cold ice clouds”. In: *J. Quant. Spectrosc. Radiat. Transfer* 112.15, pp. 2520–2525.
- Johnson, B. T., W. S. Olson, and G. Skofronick-Jackson (2016). “The microwave properties of simulated melting precipitation particles: sensitivity to initial melting”. In: *Atmos. Meas. Tech.* 9.1, pp. 9–21.
- Kahnert, Michael (2016). “Numerical solutions of the macroscopic Maxwell equations for scattering by non-spherical particles: A tutorial review”. In: *J. Quant. Spectrosc. Radiat. Transfer* 178, pp. 22–37.
- Korolev, A V, G A Isaac, and J Hallett (1999). “Ice particle habits in Arctic clouds”. In: *Geophys. Res. Lett.* 26.9, pp. 1299–1302.
- Korolev, A. V., E. F. Emery, J. W. Strapp, S. G. Cober, G. A. Isaac, M. Wasey, and D. Marcotte (2011). “Small Ice Particles in Tropospheric Clouds: Fact or Artifact? Airborne Icing Instrumentation Evaluation Experiment”. In: *Bull. Amer. Met. Soc.* 92.8, pp. 967–973.
- Korolev, Alexei and George Isaac (2003). “Roundness and Aspect Ratio of Particles in Ice Clouds”. In: *J. Atmos. Sci.* 60.15, pp. 1795–1808.

- Kuhn, Thomas and Andrew J. Heymsfield (2016). “In Situ Balloon-Borne Ice Particle Imaging in High-Latitude Cirrus”. In: *Pure Appl. Geophys.* 173.9, pp. 3065–3084.
- Kuo, Kwo-Sen, William S Olson, Benjamin T Johnson, Mircea Grecu, Lin Tian, Thomas L Clune, Bruce H van Aartsen, Andrew J Heymsfield, Liang Liao, and Robert Meneghini (2016). “The microwave radiative properties of falling snow derived from nonspherical ice particle models. Part I: An extensive database of simulated pristine crystals and aggregate particles, and their scattering properties”. In: *J. Appl. Meteorol. Clim.* 55.3, pp. 691–708.
- Latham, J. (1969). *Cloud physics*. Vol. 32. 1. IOP Publishing, p. 302.
- Lawson, R Paul, Brad A Baker, Carl G Schmitt, and T L Jensen (2001). “An overview of microphysical properties of Arctic clouds observed in May and July 1998 during FIRE ACE”. In: *J. Geophys. Res. Atmos.* 106.D14, pp. 14989–15014.
- Lawson, R. Paul, Darren O’Connor, Patrick Zmarzly, Kim Weaver, Brad Baker, Qixu Mo, and Hafidi Jonsson (2006). “The 2D-S (Stereo) Probe: Design and Preliminary Tests of a New Airborne, High-Speed, High-Resolution Particle Imaging Probe”. In: *J. Atmos. Oceanic Technol.* 23.11, pp. 1462–1477.
- Lawson, R. Paul, Ronald E. Stewart, and Leigh J. Angus (1998). “Observations and Numerical Simulations of the Origin and Development of Very Large Snowflakes”. In: *J. Atmos. Sci.* 55.21, pp. 3209–3229.
- Leinonen, Jussi, Stefan Kneifel, and Robin J. Hogan (2018). “Evaluation of the Rayleigh–Gans approximation for microwave scattering by rimed snowflakes”. In: *Q. J. R. Meteorol. Soc.* 144.S1, pp. 77–88.
- Liu, G. (2008). “A database of microwave single-scattering properties for nonspherical ice particles”. In: *Bull. Amer. Met. Soc.* 89, p. 1563.
- Lu, Yinghui, Zhiyuan Jiang, Kultegin Aydin, Johannes Verlinde, Eugene E. Clothiaux, and Giovanni Botta (2016). “A polarimetric scattering database for non-spherical ice particles at microwave wavelengths”. In: *Atmos. Meas. Tech.* 9, pp. 5119–5134.
- Lynch, D. K., K. Sassen, D. Starr, and G. Stephens, eds. (2002). *Cirrus*. Oxford University Press.
- Marshall, J. S. and W. Mc K. Palmer (1948). “The Distribution of Raindrops with Size”. In: *J. Meteorol.* 5.4, pp. 165–166.
- Mätzler, C. (2006). “Thermal Microwave Radiation: Application for Remote Sensing”. In: vol. 52. IET Electromagn. Waves Ser. Inst. Eng. Technol., Stevenage, U. K. Chap. 5.3 Microwave dielectric properties of ice, pp. 455–462.
- Maurellis, Ahilleas and Jonathan Tennyson (2003). “The climatic effects of water vapour”. In: *Phys. World* 16.5, pp. 29–33.
- May, Peter T., James H. Mather, Geraint Vaughan, Christian Jakob, Greg M. McFarquhar, Keith N. Bower, and Gerald G. Mace (2008). “The Tropical Warm Pool International Cloud Experiment”. In: *Bull. Amer. Met. Soc.* 89.5, pp. 629–646.
- McFarquhar, Greg M. and Andrew J. Heymsfield (1997). “Parameterization of tropical cirrus ice crystal size distributions and implications for radiative transfer: Results from CEPEX”. In: *J. Atmos. Sci.* 54.17, pp. 2187–2200.
- McFarquhar, Greg M. et al. (2011). “Indirect and semi-direct aerosol campaign: The impact of arctic aerosols on clouds”. In: *Bull. Amer. Met. Soc.* 92.2, pp. 183–201.

- Mie, Gustav (1908). “Beiträge zur Optik trüber Medien, speziell kolloidaler Metallösungen”. In: *Ann. Phys.* 330.3, pp. 377–445.
- Minzner, R. A. (1977). “The 1976 Standard Atmosphere and its relationship to earlier standards”. In: *Rev. Geophys.* 15.3, p. 375.
- Mishchenko, M. I., L.D. Travis, and A.A. Lacis (2002). *Scattering, absorption, and emission of light by small particles*. Cambridge, UK: Cambridge University Press.
- Mishchenko, Michael I., Larry D. Travis, and Daniel W. Mackowski (1996). “T-matrix computations of light scattering by nonspherical particles: A review”. In: *J. Quant. Spectrosc. Radiat. Transfer* 55.5, pp. 535–575.
- Mitchell, D. L., R. P. Lawson, and S. Mishra (2011). *Cirrus clouds and climate engineering: new findings on ice nucleation and theoretical basis*. INTECH Open Access Publisher.
- Mitchell, David L. and W. Patrick Arnott (1994). “A Model Predicting the Evolution of Ice Particle Size Spectra and Radiative Properties of Cirrus Clouds. Part II: Dependence of Absorption and Extinction on Ice Crystal Morphology”. In: *J. Atmos. Sci.* 51.6, pp. 817–832.
- Mitchell, David L., Renyi Zhang, and Richard L. Pitter (1990). “Mass-Dimensional Relationships for Ice Particles and the Influence of Riming on Snowfall Rates”. In: *J. Appl. Meteorol.* 29.2, pp. 153–163.
- O’Shea, S. J. et al. (2016). “Airborne observations of the microphysical structure of two contrasting cirrus clouds”. In: *J. Geophys. Res. Atmos.* 121.22, pp. 13, 510–13, 536.
- O’Shea, Sebastian J., Jonathan Crosier, James Dorsey, Waldemar Schledewitz, Ian Crawford, Stephan Borrmann, Richard Cotton, and Aaron Bansemer (2019). “Revisiting particle sizing using greyscale optical array probes: evaluation using laboratory experiments and synthetic data”. In: *Atmos. Meas. Tech.* 12.6, pp. 3067–3079.
- Ori, D., T. Maestri, R. Rizzi, D. Cimini, M. Montopoli, and F. S. Marzano (2014). “Scattering properties of modeled complex snowflakes and mixed-phase particles at microwave and millimeter frequencies”. In: *J. Geophys. Res. Atmos.* 119.16, pp. 9931–9947.
- Orikasa, Narihiro, Masataka Murakami, and Andrew J. Heymsfield (2013). “Ice Crystal Concentration in Midlatitude Cirrus Clouds: In Situ Measurements with the Balloonborne Hydrometeor Videosonde (HYVIS)”. In: *J. Meteorol. Soc. Jpn.* 91.2, pp. 143–161.
- Petty, Grant W. (2006). “A First Course in Atmospheric Radiation”. In:
- Petty, Grant W. and Wei Huang (2011). “The modified gamma size distribution applied to inhomogeneous and nonspherical particles: Key relationships and conversions”. In: *Journal of the Atmospheric Sciences* 68.7, pp. 1460–1473.
- Pfreundschuh, Simon, Patrick Eriksson, Stefan A Buehler, Manfred Brath, David Duncan, Richard Larsson, and Robin Ekelund (2019). “Synergistic radar and radiometer retrievals of ice hydrometeors”. In: *Atmos. Meas. Tech. Discuss.*
- Pruppacher, Hans R. and James D. Klett (1997). *Microphysics of Clouds and Precipitation*. 2nd ed. Kluwer Academic Publishers, Dordrecht.

- Rathsman, Torbjörn (2016). “A software toolkit for generating ice and snow particle sharp data”. MA thesis. Gothenburg, Sweden: Msc. thesis, Earth and Space Sciences, Chalmers University of Technology.
- Ray, Peter S. (1972). “Broadband Complex Refractive Indices of Ice and Water”. In: *Appl. Opt.* 11.8, p. 1836.
- Rees, W.G. (2001). *Physical principles of remote sensing*. 2nd ed. Cambridge University Press.
- Rind, D., E. W. Chiou, W. Chu, J. Larsen, S. Oltmans, J. Lerner, M. P. McCormick, and L. McMaster (1991). “Positive water vapour feedback in climate models confirmed by satellite data”. In: *Nature* 349.6309, pp. 500–503.
- Ringerud, Sarah, Mark S. Kulie, David L. Randel, Gail M. Skofronick-Jackson, and Christian D. Kummerow (2019). “Effects of Ice Particle Representation on Passive Microwave Precipitation Retrieval in a Bayesian Scheme”. In: *IEEE T. Geosci. Remote* 57.6, pp. 3619–3632.
- Rolland, Stull (2000). *Meteorology: For Scientists and Engineers*. 2nd ed. Vol. 92. Gary Garlson.
- Segeistein, David J (1981). “The Complex Refractive Index of Water”. MA thesis.
- Stephens, Graeme, David Winker, Jacques Pelon, Charles Trepte, Deborah Vane, Cheryl Yuhas, Tristan L’Ecuyer, and Matthew Lebsock (2018). “CloudSat and CALIPSO within the A-Train: Ten Years of Actively Observing the Earth System”. In: *Bull. Amer. Met. Soc.* 99.3, pp. 569–581.
- Stokes, George Gabriel (1851). “On the composition and resolution of streams of polarized light from different sources”. In: *Transactions of the Cambridge Philosophical Society* 9, p. 399.
- Storelvmo, Trude and Ivy Tan (2015). “The Wegener-Bergeron-Findeisen process – Its discovery and vital importance for weather and climate”. In: *Met. Zeit.* 24.4, pp. 455–461.
- Stubenrauch, C. J. et al. (2013). “Assessment of Global Cloud Datasets from Satellites: Project and Database Initiated by the GEWEX Radiation Panel”. In: *Bull. Amer. Met. Soc.* 94.7, pp. 1031–1049.
- Sun, Ninghai and Fuzhong Weng (2012). “Retrieval of Cloud Ice Water Path from Special Sensor Microwave Imager/Sounder (SSMIS)”. In: *J. Appl. Meteorol. Clim.* 51.2, pp. 366–379.
- Surussavadee, Chinnawat and D.H. Staelin (2009). “Satellite Retrievals of Arctic and Equatorial Rain and Snowfall Rates Using Millimeter Wavelengths”. In: *IEEE T. Geosci. Remote* 47.11, pp. 3697–3707.
- Troitsky, A. V., A. M. Osharin, A. V. Korolev, and J. W. Strapp (2003). “Polarization of Thermal Microwave Atmospheric Radiation Due to Scattering by Ice Particles in Clouds”. In: *J. Atmos. Sci.* 60.13, pp. 1608–1620.
- Um, J., G. M. McFarquhar, Y. P. Hong, S.-S. Lee, C. H. Jung, R. P. Lawson, and Q. Mo (2015). “Dimensions and aspect ratios of natural ice crystals”. In: *Atmos. Chem. Phys.* 15.7, pp. 3933–3956.
- Um, Junshik and Greg M. McFarquhar (2009). “Single-scattering properties of aggregates of plates”. In: *Q. J. R. Meteorol. Soc.* 135.639, pp. 291–304.

- Waliser, Duane E. et al. (2009). “Cloud ice: A climate model challenge with signs and expectations of progress”. In: *J. Geophys. Res.* 114.8, D00A21.
- Wallace, J. M. and P. V. Hobbs (2006). *Atmospheric science: an introductory survey*. Vol. 92. Academic press.
- Warren, Stephen G. (1984). “Optical constants of ice from the ultraviolet to the microwave”. In: *Appl. Opt.* 23.8, p. 1206.
- Warren, Stephen G and Richard E Brandt (2008). “Optical constants of ice from the ultraviolet to the microwave: A revised compilation”. In: *J. Geophys. Res.* 113.D14, p. D14220.
- Waterman, P.C. (1965). “Matrix formulation of electromagnetic scattering”. In: 53.8, pp. 805–812.
- Webster, P. J., V. O. Magaña, T. N. Palmer, J. Shukla, R. A. Tomas, M. Yanai, and T. Yasunari (1998). “Monsoons: Processes, predictability, and the prospects for prediction”. In: *J. Geophys. Res. Ocea.* 103.C7, pp. 14451–14510.
- Westbrook, C. D., R. C. Ball, P. R. Field, and A. J. Heymsfield (2004). “Theory of growth by differential sedimentation, with application to snowflake formation”. In: *Phys. Rev. E* 70.2, p. 021403.
- Wu, D.L., J.H. Jiang, and C.P. Davis (2006). “EOS MLS cloud ice measurements and cloudy-sky radiative transfer model”. In: *IEEE T. Geosci. Remote* 44.5, pp. 1156–1165.
- Wylie, Donald, Darren L. Jackson, W. Paul Menzel, and John J. Bates (2005). “Trends in Global Cloud Cover in Two Decades of HIRS Observations”. In: *J. Climate* 18.15, pp. 3021–3031.
- Xie, Xinxin, Ulrich Löhnert, Stefan Kneifel, and Susanne Crewell (2012). “Snow particle orientation observed by ground-based microwave radiometry”. In: *J. Geophys. Res. Atmos.* 117.D2.
- Xu, Yu-lin (1995). “Electromagnetic scattering by an aggregate of spheres”. In: *Appl. Opt.* 34.21, p. 4573.
- Yang, Ping and K. N. Liou (1996). “Geometric-optics–integral-equation method for light scattering by nonspherical ice crystals”. In: *Appl. Opt.* 35.33, p. 6568.
- Yang, Ping and K. N. Liou (1998). “Single-scattering properties of complex ice crystals in terrestrial atmosphere”. In: *Contributions to atmospheric physics* 71.2, pp. 223–248.
- Yurkin, M. A. and A. G. Hoekstra (2014). *User Manual for the Discrete Dipole Approximation Code ADDA 1.3b4*.
- Zhang, K., X. Liu, M. Wang, J. M. Comstock, D. L. Mitchell, S. Mishra, and G. G. Mace (2013). “Evaluating and constraining ice cloud parameterizations in CAM5 using aircraft measurements from the SPARTICUS campaign”. In: *Atmos. Chem. Phys.* 13.9, pp. 4963–4982.